# LASER-INDUCED GRAPHENE-BASED TRANSIENT CIRCUITS FOR FLEXIBLE AND RECYCLABLE ELECTRONICS

AREF SOLTANI TEHRANI

A THESIS SUBMITTED TO THE FACULTY OF GRADUATE STUDIES IN PARTIAL FULFILLMENT OF THE REQUIREMENTS FOR THE DEGREE OF

MASTER OF APPLIED SCIENCE

GRADUATE PROGRAM IN MECHANICAL ENGINEERING

YORK UNIVERSITY
TORONTO, ONTARIO

DECEMBER 2022

# Abstract

Transient electronics are electronic devices with the ability to disintegrate/dissolve in a programmable manner, usually over a short period of time. Their by-products, after any dissolution, are usually harmless and benign, and hence they are an attractive approach to the global e-waste problem, especially for low-cost, one-time-use devices such as RFID tag antennas. This thesis focuses on designing and fabricating transient circuits with descent mechanical and electrical properties. To aim this, a laser is used to carbonize thin films made of nature-derived Lignin and graphene oxide. SEM, XPS, and Raman spectroscopy are used to study morphology and chemical composition of the films. Having optimized the material composition and laser parameters using four-point probe measurement, an RFID tag is designed and fabricated as a proof-of-concept. In the end, the transient property of the circuit is tested by dissolving the tag in water.

*To*

*my loving wife, family, and friends*

# Acknowledgments

# Table of Contents

# List of Figures

# List of Tables

# List of Acronyms

| | |
|---|---|
| GO | Graphene Oxide |
| Na-LgS | Sodium Lignosulfonate |
| 30 GO | 30% GO and 70% Na-LgS |
| SEM | Scanning Elec |
| XPS | X-ray Photoelectron Spectroscopy |
| DMM | Digital Multimeter |
| PET | Polyethylene terephthalate |
| RFID | Radio Frequency Identification |

# List of Symbols

| | |
|---|---|
| R | Resistance |
| $R_s$ | Sheet Resistance |
| V | Voltage |
| $\Psi, \Phi$ | Magnetic Flux |
| L | Inductance |
| $l_c$ | Total Length |

# 1 Introduction

In this chapter, an overview of the problem this research aims to solve, and its potential solution, followed by an introduction to the materials used in this research are provided. Then, the manufacturing method that was used in this research, called Laser Carbonization, is described. In the end, the literature review is discussed in order to find the gap in research and illustrate the contribution of this research.

## 1.1 E-waste - a Global Problem

The last decade has witnessed a sharp rise in the manufacturing and use of electrical and electronics equipment (EEE), which has raised concerns about the electronic waste (e-waste) that's associated with cheap and single or few-use electronics. Based on the latest statistics reported by United Nations University (UNU), in 2016 and 2020, almost 44.7 and 52.2 million metric tons (Mt) of e-waste were created worldwide, respectively [1]. Unfortunately, Canada and USA are significant contributors to this problem by producing on average 20 kg/inhabitant of e-waste in 2016, meaning that Canada produced roughly, 0.72 Mt of e-waste that year[1]. The e-waste is caused due to the presence of hazardous, xenobiotic (human-made) materials in daily-use EEE products. "Reducing waste" is one of Canada's goals toward 2030 future sustainability under the Paris agreement, which is a legally binding international treaty on climate change adopted in 2016 [2]. Based on this plan, products need to become more sustainable and more 'circular' to reduce waste. Radio-frequency identification (RFID) tags are an example EEE product with a single or few use requirement that are often discarded without any concern for reuse, recycling or the environment. RFID smart tags are used for high-volume, mass-use applications such as transit tickets, retailing and food labels, and packaging industry, etc. Lack of eco-friendly materials - mostly fossil fuel-derived plastics and metal foils - used in conventional tags, along with material separation costs means that these parts have had a polluting environmental presence for many years.

## 1.2   Transient Electronics – a Promising Solution

Recycling single or few-use electronics is economically not feasible due to the low-cost of raw materials for new electronics, while at the same time older electronics have higher costs for separating the integrated materials. Hence, they are usually discarded into the environment and end up in landfills or polluting the environment with their hazardous, xenobiotic (human-made) materials [3].

Transient Electronics, which refers to a type of eco-friendly electronic device that has the ability to disintegrate in a predefined environment while leaving no harmful material, is a promising solution to this ecological problem [4], [5]. Recently, such technology has been widely studied for implementation in several fields such as medical, bioengineering, energy, electronics, and sensors [6]–[11]. For example, Rasel et al. [12] developed a quick, one-step reduction process of graphene oxide (GO) using a metal substrate, with the ability to functionally grade the deposited films from insulating GO on one side to a conductive reduced-GO on the other side. The inherent water-dispersibility of GO facilitates the dissociation of the electronically conductive films in water to create a homogenous recyclable suspension. In another study by Kwon et al. [11], a recyclable conductive composite material made of polycaprolactone (PCL), silver fillers, and enzyme/protectant nanoclusters is introduced to be used for printed transient electronics, which could be degraded in warm water. Roughly 94% of the decomposed materials can be reused to fabricate electronics possessing the same functionality.

## 1.3　Materials

### 1.3.1　Graphene

In 2004, Novoselov et al. [13] used a mechanical peeling technique to successfully detach graphene from the monolithic state, which put the theory of two-dimensional crystals to the test. A planar hexagonal lattice makes up the structure of graphene. Each carbon atom has four valence electrons, including three (2s, 2px, and 2py) electrons that create planar $sp^2$ hybrid orbitals. The last orbital electron creates a strong $\pi$ bond and is free to move though the plane. It has a hexagonal honeycomb crystal structure and is a two-dimensional carbonaceous substance. With a sheet thickness of 0.34 nm, graphene is the thinnest and most durable nanomaterial available today [14]. Graphene has a fairly stable structure with a short C-C bond length (0.142 nm) [15]. There is no scattering phenomena because of interference from external atoms or lattice defects when the electrons travel in the internal orbits [16], [17]. Graphene has several fantastic properties, such as high electrical conductivity ($10^6$ S/m) and high mechanical stiffness (Young's modulus of 1 TPa), as a result of its unique planar lattice structure [18]. Graphene may be produced in a variety of ways nowadays, but the most common ones include mechanical and liquid phase exfoliation, chemical vapor deposition, epitaxial growth, and redox techniques [19].

### 1.3.2　Graphene Oxide and its Reduction

Graphene oxide is a two-dimensional carbon compound with polydisperse sheet sizes and a single atomic layer and is known as the oxidized form of Graphene. The benefits of graphene oxide (GO) over graphene are inexpensive production costs, mass production,

and simple processing [20]. Because graphene oxide has oxygen-containing functional groups, the structure of graphene oxide is more complex, and the characteristics of graphene oxide are influenced by its structure [21]. The hexagonal carbon structure of GO is comparable to that of graphene, but it additionally includes functional groups based on oxygen, such as hydroxyl (-OH), alkoxy (C-O-C), carbonyl (C=O), carboxylic acid (-COOH), and others. These oxygen-containing groups or decreased doping components can be utilized as catalytic active centers for covalent or non-covalent modification design in accordance with the specifications of certain application fields. The graphene oxide interlayer gap is also widened by the presence of groups that contain oxygen. The L-K model, created by Lerf, describes the structural characteristics of graphene oxide [22]. It is shown that the carboxyl and carbonyl groups are added to the edge of the single layer of graphene oxide, but the hydroxyl and epoxy groups are arbitrarily dispersed over the basal plane of GO.

In most cases, sheet peeling, and oxidant intercalation are the two steps used to prepare graphene oxide. Through this method, first graphite is oxidized using various reagents (e.g., $HNO_3$, $KClO_3$) which produces oxygen functional groups on the graphene-like sheets. Then, the oxidized sheets are exfoliated resulting in the production of graphene oxide 2D sheets. The exceptional structural and morphological characteristics of graphene and graphene oxide result in their superior electrical, mechanical, and thermal properties [23]–[25].

By eliminating the functional groups through various reduction methods such as (electro)chemical [20], thermal [26], hydrothermal [27], and photothermal [28], GO can

be converted into electrically conductive graphitic carbons, commonly referred to as reduced graphene oxide (rGO) (See Figure 1.1).
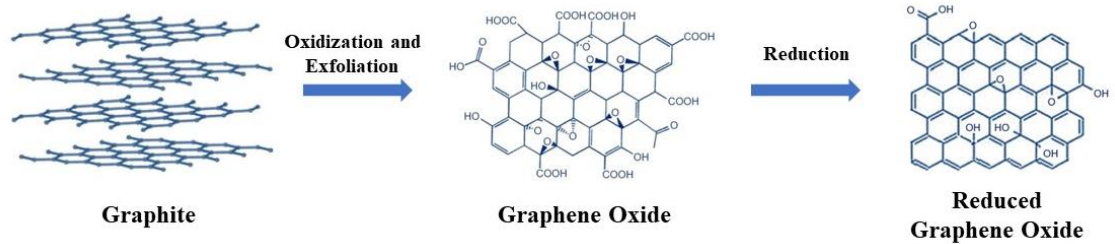


*Figure 1.1 From Graphite to reduced Graphene Oxide.*

Numerous research has been conducted on Graphene Oxide reduction methods ranging from chemical and thermal to complex approaches such as electrochemical and laser-assisted methods. Pei et al. [29] reported a Hydroiodic (HI) Acid-assisted method for Graphene Oxide reduction, which showed a C/O ratio above 12. The low sheet resistance (1.6 kohm/sq) of the fabricated rGO films, which is particularly lower than other previous chemical methods, verifies the considerable effect of HI Acid in GO reduction. Furthermore, it has been reported that a laser beam can efficiently reduce GO films on an arbitrary substrate [20]. Regarding the research conducted on Laser-induced graphene oxide reduction, Guan et al. [30] have reduced the GO using a laser beam to achieve a high conductivity (727 S m$^{-1}$) on the reduced parts. Huang et al. [31] have shown that GO can be considerably reduced and self-assembled when in contact with a metal (e.g., Aluminum) powder or sheet. For example, a wide graphene film was fabricated in the presence of copper foil at a high temperature of 900 °C followed by annealing in an H2-containing atmosphere. The electrical properties of the metal-assisted reduced films (3.6x10$^4$ S/m) show promising potential in flexible electronics applications.

6

### 1.3.3   Sodium Lignosulfonate

Biomass (wood and nonwood), whose three primary components are cellulose, hemicellulose, and lignin, is one of the most abundant and renewable resource in the world. The most prevalent biopolymer in woody biomass is cellulose, followed by lignin, which accounts for 15-40 wt% of wood [32]. Lignin is the most abundant natural source of aromatic chemicals [33]. However, just 1-2% of the 50-70 million tons of lignin produced each year is used to make any value-added products, implying that it is an underused resource. Lignin can be sulfonated to Lignosulfonate, and because of the presence of the sulfonated group, lignosulfonates are anionically charged and water soluble. Because of their unique properties, lignosulfonates have a wide range of applications, including animal feed, insecticides, surfactants, additives in oil drilling, colloidal suspension stabilizers, and as plasticizers in concrete admixtures [34].

## 1.4   Laser Carbonization

Carbonization has traditionally been accomplished using pyrolysis or hydrothermal techniques [35]. The resulting products and their qualities are a direct result of the precursors, the reaction circumstances (such as temperature, pressure, time, or the presence of reactants in the synthesis environment), and the synthesis environment. In this regard, so-called laser-carbonization offers an opportunity to expand the area of film-based electronics for carbonized materials. In general, laser-induced or -assisted synthesis, which is not confined to carbon, has piqued the interest of many materials scientists [36].

Laser-fabrication methods have been widely used as facile, cost-effective, and energy-efficient techniques for both research and industrial purposes [36]. With regard to carbon materials synthesis, in the 1990s, lasers were widely investigated as energy sources for the production of carbon nanomaterials [37]. Generally, such photo-thermal syntheses differ from traditional thermal methods, with the reaction time occurring instead in micro- or milliseconds [38]. Being accurate and controllable, the aforementioned technologies have been implemented in fabrication of biosensors [39], [40], mechanical sensors [41], [42], and energy storage and supercapacitors [43]–[45] using various precursors such as biomaterials, polymers, and organic materials [46], [47].

## 1.5  Literature Review – Laser Carbonization

Last decade has witnessed numerous research carried out in laser manufacturing of flexible electronics. In this section, some of the most recent and popular works are summarized. El-Kady et al. [48], demonstrated scalable manufacturing of graphene micro supercapacitors over huge regions utilizing a common LightScribe DVD burner and direct laser writing on graphite oxide films with a conductivity of $2.35 \times 10^3$ S m$^{-1}$. These micro-supercapacitors have a power density of 200 W cm$^{-3}$, which is among the highest values attained by any supercapacitor. In another study conducted in Prof. James Tour's group, Laser induction is used to create 3D porous graphene sheets from polymers [49]. Using a commercial CO$_2$ laser, a Polyimide (PI) film was graphitized to achieve a sheet resistance of less than 15 $\Omega$/sq. Following the previous work, Liu et al. [50], presented a high-efficiency method for fabricating Fe$_3$O$_4$ nanoparticle-anchored laser-induced graphene (LIG/ Fe$_3$O$_4$) with hierarchical porous structures on a flexible PI substrate, in which

aggregated $Fe_3O_4$ nanoparticles (24.08 nm) with mesopores are laser-deposited onto macroporous LIG scaffolds in one step, resulting in conductivity of 17.16 S cm$^{-1}$. In addition, in another work by Zhang et al. [45], a simple lignin-based laser lithography approach is developed and utilized to build on-chip micro-supercapacitors (MSCs) with 3D graphene electrodes. A straightforward one-step $CO_2$ laser irradiation converts lignin sheets directly into 3D laser-scribed graphene (LSG) electrodes. The obtained LSG electrodes are porous in a hierarchical manner, with an electrical conductivity of up to 66.2 S cm$^{-1}$ and a high specific surface area of 338.3 m$^2$ g$^{-1}$. Furthermore, Kulyk et al. [51], fabricated strain and bending sensors made by irradiating standard filter paper with a $CO_2$ laser. The developed material has porous electrically conductive weblike structures with sheet resistances as low as 32 $\Omega$/sq. These devices have shown reliable real-time response to the given physical parameters, confirming graphene's promise for low-cost and environmentally friendly sensing devices. In another recent work presented by Yuan et al. [52], an efficient, simple, and scalable strategy for producing in situ heteroatom-doped porous graphene via laser direct writing on a precursor-doped polyimide (PI) film was proposed. This work was conducted for the first time by combining PI powder and precursors with a sodium carboxymethyl cellulose (CMC) binder via a drop-casting and low-temperature drying process, implying a conductivity of 39.5 S cm$^{-1}$. Also, in another research carried out by this group, kraft Lignin was used as the precursor to fabricate laser-induced graphene films for flexible supercapacitors application [53].

## 1.6 Research Objectives and Contribution

Most of the laser carbonization precursors used in the literature are relatively expensive and non-renewable, while polymeric materials limit the resulting material properties. To overcome this challenge, bio-based materials, like lignin and its derivatives, are being studied as safe, inexpensive, and readily accessible substitutes. Tour's group has shown an achievable high conductivity through the low-cost method of converting wood into so-called laser scribed graphene (LSG) using a $CO_2$ laser under a special atmosphere [49]. In another work carried out by Lei et al. [54], highly conductive LSG was obtained by MXene-based spray coating of carbonized lignin/PVA/urea composite for sensing applications. Despite showing promising materials/approaches to creating transient electronics, the existing approaches are limited in real-world functionality with either poor mechanical and electrical properties or require a complex and time-consuming manufacturing process.

To bridge this gap, we took advantage of the inherent biodegradability and transient properties of natural, carbon-based GO and lignins to fabricate transient electronics which meet the required electrical and mechanical properties. In this regard, we defined an objective triangle, each vertex showing a prominent characteristic (Figure 1.2). First, the fabrication process should be fast, simple, and able to create complex shapes as most electronic circuits require obtaining complicated geometries. Second, the fabricated circuit should possess high conductivity to effectively function as an electronic circuit, especially a contactless RFID antenna. Third, the circuits should demonstrate flexibility

to endure bending cycles when used as wearable electronics or flexible RFID-based single-use products.
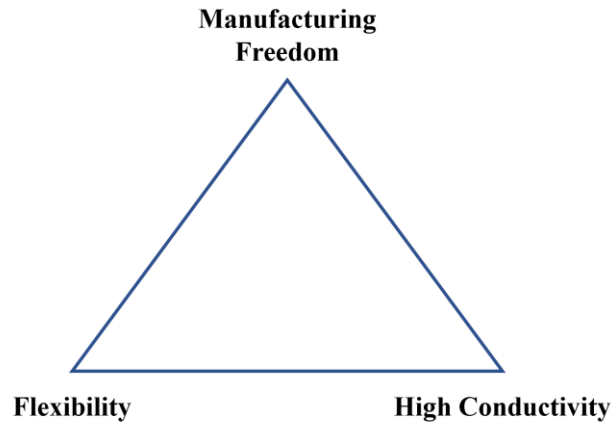


*Figure 1.2  Schematics of objectives triangle. The top vertex refers to the manufacturing method ability to create complex shapes and others demonstrate the properties that the fabricated film should possess.*

In this regard, GO – an abundant, oxidized form of graphene – as the base material and sodium lignosulfonate (Na-LgS) were chosen. Na-LgS, a well-known strong binder for cellulose in trees, was used as the adhesive to prevent GO sheets from peeling off caused by off-gassing during laser carbonization (see section 3.1). As for a fast, inexpensive, and flexible design manufacturing process, laser-carbonization has been chosen for its numerous advantages. First, laser processes are highly controllable through varying parameters like laser speed, power, and beam focus height and wavelength. Second, the high energy of the laser beam is able to break the chemical structure and carbonize numerous carbon-based precursor materials and make them conductive.

In this thesis, a laser with various parameters is implemented to carbonize different compositions of the GO/Lignin films to create and optimize highly-conductive transient

electronics. To characterize the properties, Scanning Electron Microscopy (SEM), Raman Spectroscopy, and X-ray Photoelectron Spectroscopy (XPS) were performed, which revealed the morphology and carbonization level of the samples. Then, four-point probe measurements were performed on samples to measure the sheet resistance. In addition, cyclic bend testing was used to measure the resistance of the films upon repeated loading and unloading. Having the composition and laser parameters optimized, a coil-shaped RFID tag is designed, optimized, fabricated, and tested as a proof-of-concept. Last but not least, the film was immersed in water to demonstrate the transience and disintegration properties, with the film-degradation performance characterized over time.

## 1.7   Organization

This thesis is organized into six chapters. Chapter 2 presents the materials and methods used for this research. The solution preparation of each material and then preparation of the composite and laser carbonization process are elaborated in detail. Furthermore, the instruments used for fabrication and characterization are introduced. In chapter 3, the results of the morphology study of the different laser-treated primary films using SEM, Raman and XPS spectroscopy are provided. In Chapter 4, the electrical properties of the laser-carbonized films are optimized for material composition and laser parameters. Moreover, the electrical conductivity of the laser-scribed films was studied under bending loading. Chapter 5 is dedicated to the illustration of the project's real-life application, Radio Frequency Identification (RFID) tag, and its transient property. Finally, chapter 6 summarizes the results of the research and recommendations for future work.

# 2 Material Preparation and Laser Carbonization Process

Chapter 2 discusses the materials and instruments used to fabricate and characterize the transient electronic films, followed by a step-by-step recipe for the laser carbonization process. The solution preparation of each material and then preparation of the composites are elaborated on in detail. Having prepared the precursor, then the method and steps of fabricating the films are explained. In the end, the laser carbonization process of different compositions is explained.

## 2.1 Experimental Section

### 2.1.1 Material Preparation

Highly concentrated Graphene Oxide and Sodium Lignosulfonate materials (Figure 2.1) were used in this study to fabricate the films on Polyethylene Terephthalate (PET). GO dispersion (2.5 wt%) was purchased from Graphenea Inc, Spain. Based on the company's report, the material properties include a D90 particle size of 29-33 μm and >95% monolayer content measured in 0.05 wt% aliquot. Na-LigS used in this work was purchased from Borregaard, Norway. The PET substrate with a thickness of 170 μm was with the tradename of Melinex obtained from Plano GmbH.



*Figure 2.1  Precursor materials used in this research: Graphene Oxide (left) and Na-Lignin (right).*

### 2.1.2 Preparation of GO/Na-LigS precursor

GO (2.5 wt%) was concentrated to 3.5 wt% by removing the water from the dispersion through heating the material in a beaker and on a hotplate stirrer at 40ºC while slowly

stirring. Na-LigS solution (50 wt%) was prepared by gradually adding the Na-LigS powder to deionized water whilst stirring at room temperature. The GO concentration process is necessary to make a gelous precursor to be coated on the substrate. Then, two materials were mixed and stirred at room temperature for 2 h to obtain a homogenous suspension. 30GO, which stands for 30% GO and 70% Na-LigS solidified film, was obtained by mixing and drying a specific amount of the suspensions in a way that a 30% GO powder/Na-LigS powder weights ratio was obtained.

### 2.1.3 Preparation of the GO/Na-LigS films

The prepared gelatinous solution was used as a carbon-based precursor ink. An adequate amount of ink was doctor bladed on the PET substrate with a wet thickness of 300 μm. The assembly was then placed on a hotplate for 2h at 60ºC to make a ~20 μm-thick dry film.

### 2.1.4 Fabrication and Characterization Instruments

A Zeiss LEO 1550-Gemini (acceleration voltage 3 to 10kV) was used for Scanning Electron Microscopy. Raman spectra were determined by a confocal Raman Microscope (alpha300, WITec, Germany) where the laser with the wavelength of 532 or 785 nm and power of 1 mW was focused on the sample through a 20× objective. XPS spectra was obtained on Thermo Fisher Scientific K-Alpha (Thermo Fisher Scientific, E. Grinstead UK). Sheet Resistance measurements were carried out using a customized setup and a Signatone SP4-62045TBJ four-point probe with 0.0625-inch tip spacing.

Bending studies were carried out using a homemade force table. At a distance of 25 mm, the sample strip was secured by two opposing copper electrode clips, one of which was coupled to a moveable table. To improve electrical contact, both ends of the carbon strip were silver painted and linked to the copper electrodes. The bending curvature was measured by converting the forms from pictures into x-y data with the freeware Engauge Digitizer. Curvature is defined as the inverse radius at the point of maximum bending. Resistance was measured in four-point geometry in all tests using an RS PRO RSDM3055A digital multimeter and Matlab-based software. Figure 2.2 shows the bending setup.

The Snapmaker 2.0, A350T 3in1 machine, equipped with a 1600 mW blue laser with a wavelength of 450 nm, was used to print carbonized patterns on the film (Figure 2.3). The adjustable parameters for the laser machine are power (%) and speed (mm/min).
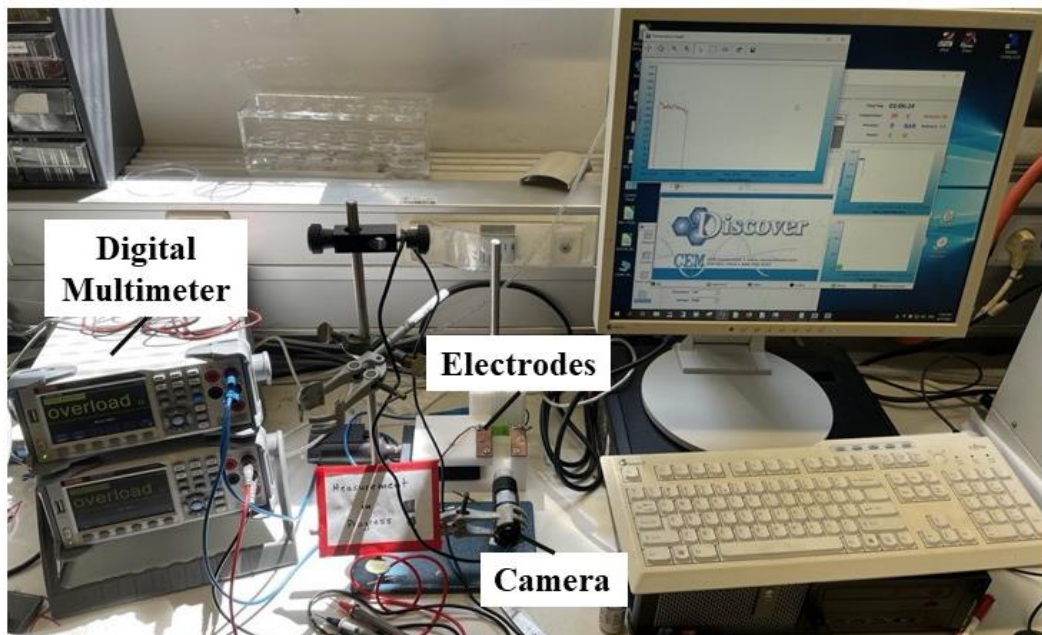


*Figure 2.2  Bending setup components description.*
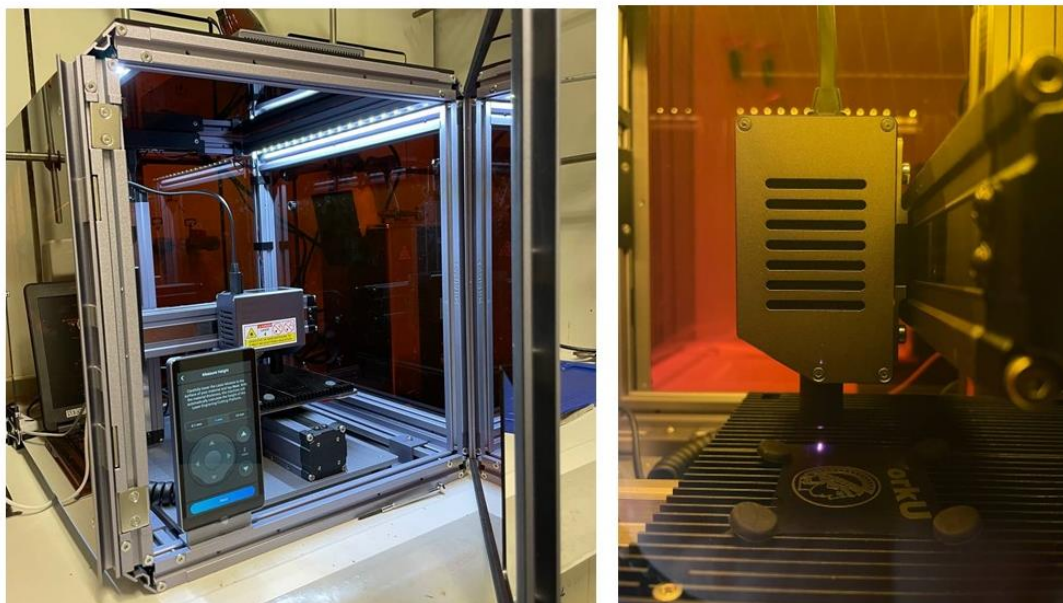
*Figure 2.3  The Snapmaker 2.0, A350T 3in1 laser machine.*

## 2.2   Laser Carbonization Process

### 2.2.1   Film Preparation

The details of the fabrication process of laser-induced films are demonstrated in Figure 2.4. First, a homogeneous Na-Lignosulfonate (NaLgS)/graphene oxide (GO) suspension was prepared, as explained in section 2.1.2., and uniformly coated on the polyethylene terephthalate (PET) substrate using a doctor blade coating (step 1). The thickness of the coated material can be controlled by two micrometers attached to the blade which identifies the height of the blade from the substrate surface (Figure 2.5A).
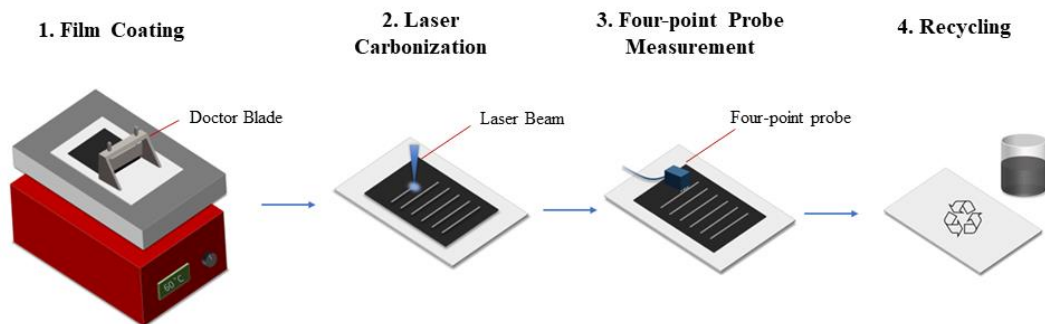
*Figure 2.4  Schematic drawings of primary film preparation, laser carbonization/reduction, four-point probe sheet resistance measurement, and water-assisted recycling process.*

After drying on a hotplate at 50 °C for 1 hour, the assembly was exposed to a blue laser ($\lambda = 450$ nm) to carbonize a series of simple lines for electrical conductivity measurements (step 2). An optical microscope image of the precise laser-carbonized sample lines is shown in Figure 2.5B. It is known that laser patterning can be implemented to precisely pattern complex shapes, like a coil shape pattern (for use in RF-ID antennas) or York University and Max Planck Institute logos, as demonstrated in Figure 2.5C.

The sheet resistance of the carbonized part was measured using a four-point probe head, as shown in Figure 2.4, step 3. By taking advantage of the high water-dispersibility of Na-LigS and GO, the assembly can be easily disintegrated in water to have the PET substrate either recycled or reused, as shown in Figure 2.4, step 4. Although the laser-carbonized parts cannot be dissolved in water, they are broken down into tiny pieces over time upon the disintegration of the close-by unexposed primary film, followed by being completely removed from the PET surface over time.
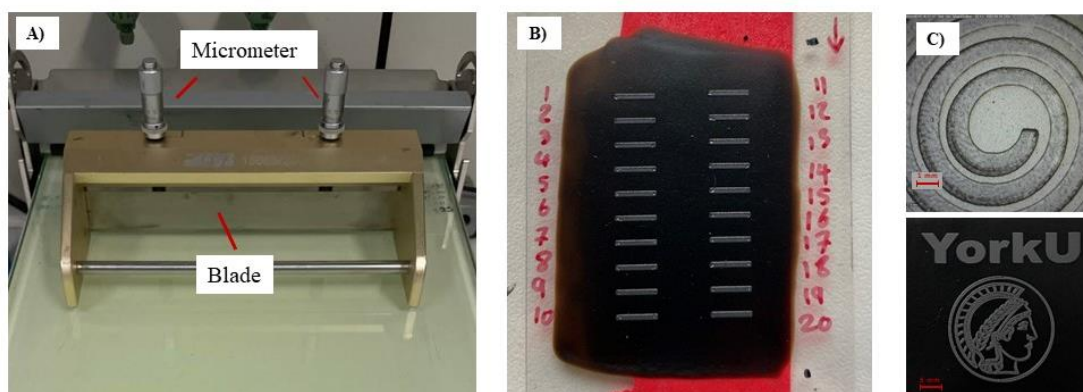
*Figure 2.5 A) Doctor Blade Coater, B) laser scribed samples, C) coil-shaped and logos printed with laser.*

As shown in previous literature [55]' [56], GO-flakes tend to align vertically after the laser-assisted reduction process due to $CO_2$ and $H_2O$ off-gassing. This causes a decrease in in-plane electrical conductivity due to an increase in sheet-to-sheet contact resistance [57]. To address this problem, Na-LgS was chosen as an additive because of its binder-like properties as well as its high effective carbonization yields and high achievable electrical conductivity [45], [58]. To investigate the effect of Na-LgS on the morphological structure and electrical properties, aqueous suspensions of GO and Na-LgS with various compositions were tested for primary films. GO and Na-LgS are well-known for their superior water solubility as a result of a substantial amount of available oxygen functional groups and sulfuric acid, respectively. Homogenous dispersions of GO/Na-LgS were prepared by mixing the specific mass ratio of aqueous solutions of GO (3.5 wt%) and Na-LgS (50 wt%) to produce samples with varying mass fractions of GO. Table 2.1 provides an overview of the different compositions and sample names.

*Table 2.1  A list of used concentrations of GO and Na-LgS with sample.*

| Sample | c(GO) (mg mL$^{-1}$) | c(Na-LgS) (mg mL$^{-1}$) | m(GO) (mg cm$^{-2}$) | m(Na-LgS) (mg cm$^{-2}$) | Mass fraction of GO (wt%) |
|---|---|---|---|---|---|
| GO | 35 | 500 | 50 | 0 | 100 |
| NaLgS(40)/GO(60) | 35 | 500 | 30 | 20 | 60 |
| NaLgS(50)/GO(50) | 35 | 500 | 25 | 25 | 50 |
| NaLgS(60)/GO(40) | 35 | 500 | 20 | 30 | 40 |
| NaLgS(70)/GO(30) | 35 | 500 | 15 | 35 | 30 |
| Na-Ligns | 35 | 500 | 0 | 50 | 0 |

## 2.3   Coating on Paper-Based Substrates

Although PET is a recyclable material, as commonly observed in plastic water bottles, it is not biodegradable. Biodegradability refers to a type of materials that are able to break up when exposed to the presence of microorganisms. In this regard, we tried to replace the PET substrate with other off-the-shelf films. Figure 2.6A shows the paper-based substrate on which GO/Na-LgS is coated. Due to the high hydrophilicity attribute of the conventional papers and the high amount of water in the material composition (~95wt%), the paper as substrates tend to get distorted. The distortion that emerged in the paper, hence, affects the laser carbonization process in terms of the distance between the laser nozzle and the film, known as laser focus. To be more specific, hill-shaped parts of the sample undergo underfocused laser beam while the other parts experience an overfocused laser beam as exhibited in Figure 2.6B. The defocused laser beam affects the level of carbonization since the amount of energy per area delivered by the laser is highly dependent on laser focus, according to James Tour's report [59]. As a result, obtaining uniform carbonization throughout the paper-coated films seems impossible using

conventional laser machines since controlling the laser parameters, especially laser focus, is vital in terms of controlling the carbonization process.

In order to overcome this challenge, we used labeling tapes as the substrate as shown in Figure 2.7. The tape showed a stable performance with regard to reducing the distortion upon coating. This could be attributed to the wax coated on the tape which prevents the paper layer from absorbing the water from the material. Furthermore, the glue on the opposite side of the tape tends to maintain the structure of the paper. To prove the laser carbonization performance of the tape-coated film, the electrical conductivity of the carbonized line was measured and compared with the same material coated on PET, which resulted in the same electrical conductivity. Moreover, as is obvious in Figure 2.7, the tape-coated sample is able to withstand bending caused by hand.
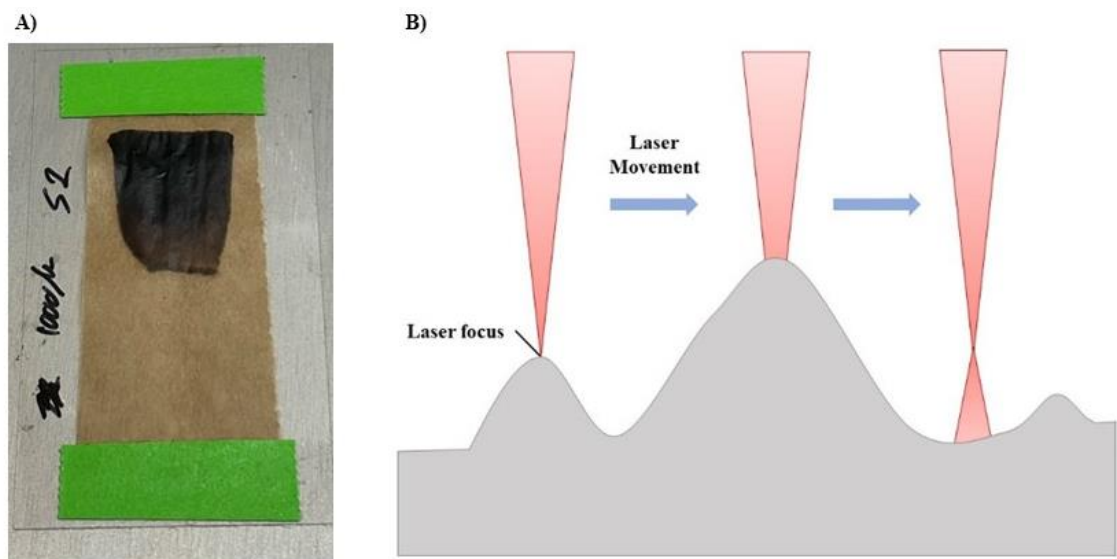


*Figure 2.6  A) GO/Na-LgS coated on a paper-based substrate, B) schematics of defocused laser beam on film distorted surface.*
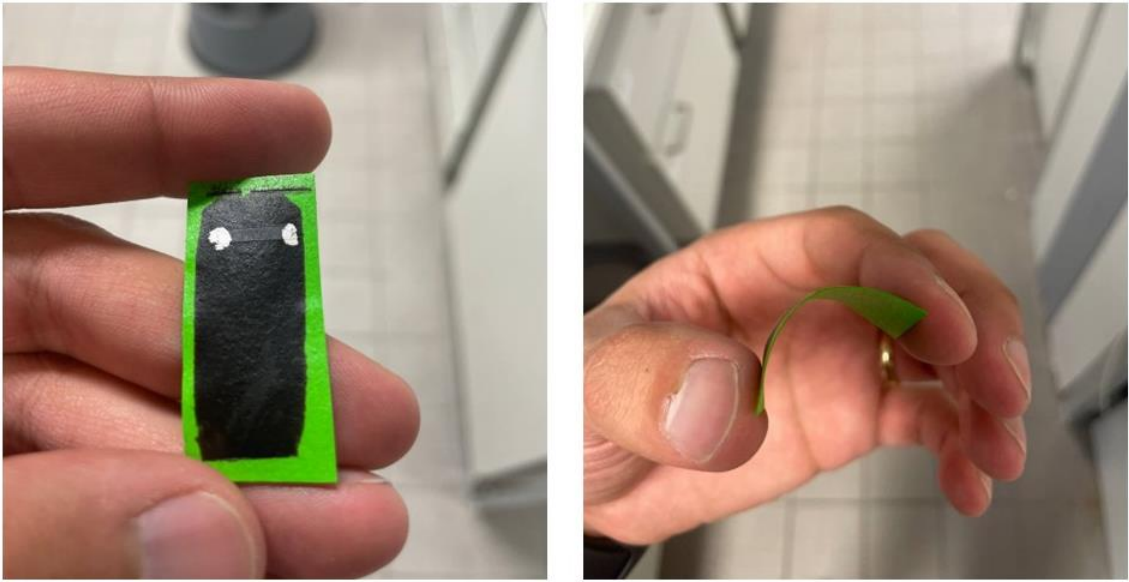
*Figure 2.7  Optical images of GO/LgS coated on a labeling tape showing the same performance compared to the sample coated in PET.*

# 3 Morphology and Chemical Characterization of Laser-Carbonized GO/Na-LgS

In this chapter, the results of the morphology study of the different laser-treated primary films are provided. In short, Scanning Electron Microscopy (SEM) was used to study the morphology of the materials before and after carbonization process. Then, Raman and X-ray Spectroscopy was used to study and compare the level of carbonization of each recipe according to their chemical compositions.

## 3.1  Scanning Electron Microscopy (SEM)

Cross sectional and top view SEM images of the pure GO samples coated on a PET substrate are shown in Figure 3.1. The images show a homogenous and flat surface of the GO. This can be attributed to the coating method, doctor blading, though which a blade uniformly coats the material. Figure 3.2 shows the cross-sectional SEM image of laser-reduced primary film consisting of pure GO where the laser-reduced GO flakes are partially vertically arranged, as discussed earlier. While the concentrated high-energy laser beam hits the GO sheets, the flakes tend to expand and face up from one edge creating an "L" shape due to the instantaneously high absorbed thermal energy [60]. This is due to the high-energy reduction process where oxygen functional groups are removed from the surface to generate gases such as CO and $CO_2$. Based on the thermodynamics equation of state, the built-up pressure caused by the gas exhaust at ~1000 °C is estimated to be 130 MPa, while the required pressure to separate two GO sheets is approximately 2.5 MPa [61].
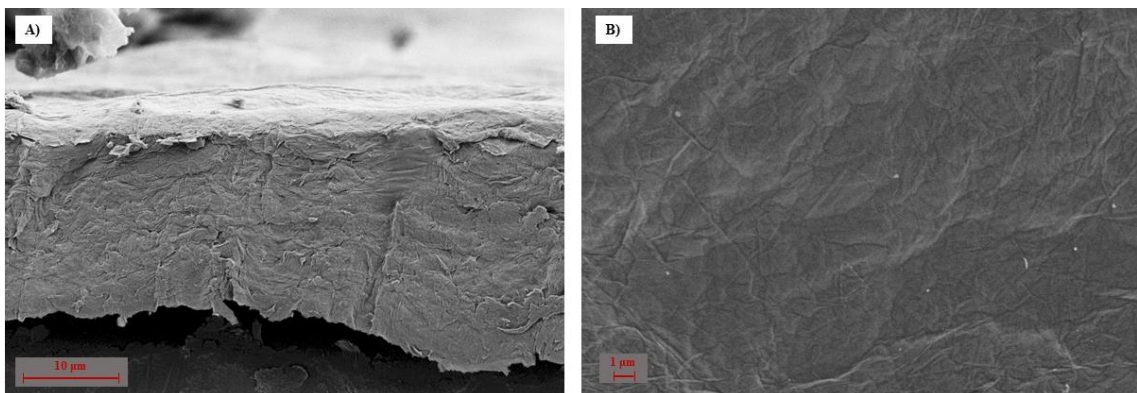


*Figure 3.1  A) Cross sectional and B) top SEM images of the pure GO coated on PET.*
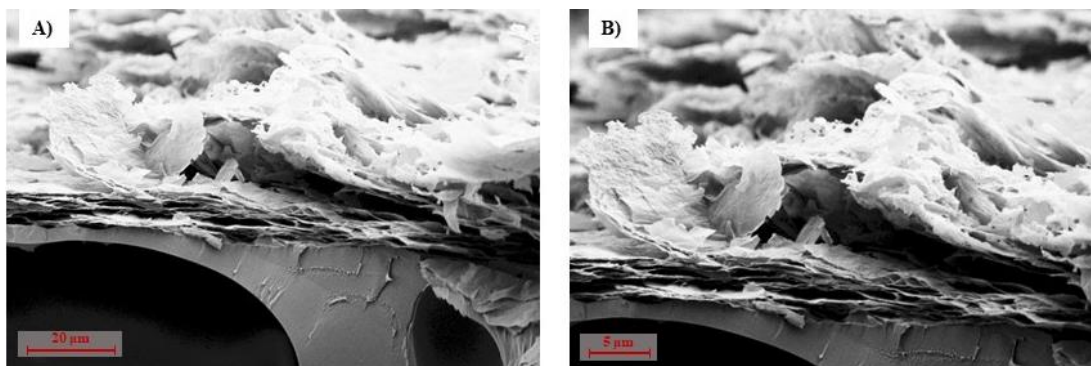
*Figure 3.2   Cross sectional SEM images of the reduced GO.*

In addition, at the optimized laser parameters (see Experimental Section) for obtaining the lowest sheet resistance, it is observed that the PET substrate melted due to GO's high energy absorption at the laser wavelength. As a reference, Figure 3.3 shows the cross-sectional SEM image of laser-carbonized Na-LgS. The obvious coarse morphology shows the micro/macropores generated due to the gas diffusion during the laser process – e.g., $H_2O$ and $CO_2$. The above discussion demonstrates the morphological effect in laser-carbonized pure GO and Na-LgS, either of which tends to reduce the in-plane conductivity by increasing the sheet-to-sheet contact resistance and the amount of porosity (tortuosity) of the electron conducting pathway.
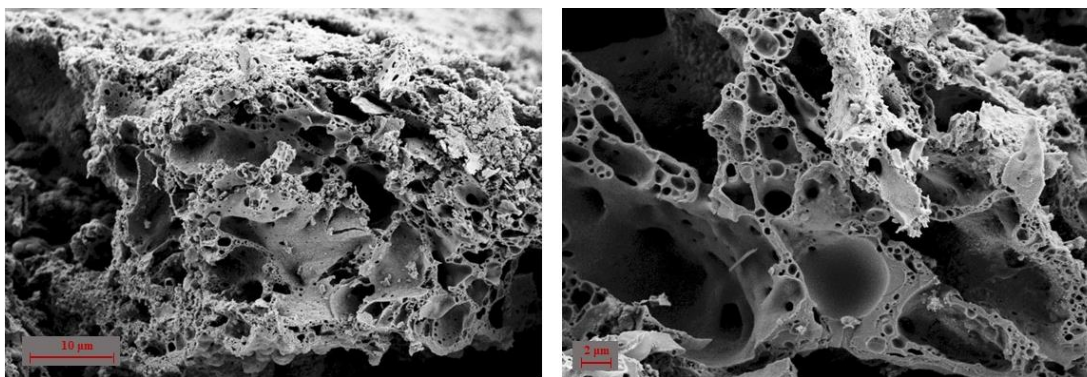


*Figure 3.3  Cross sectional SEM images of the reduced Na-LgS.*

25

Surface and cross-sectional SEM images of the dried 30GO film demonstrate that GO sheets were evenly dispersed in Na-LgS while aligning horizontally and sticking on top of each other by the inherent adhesive effect of Na-LgS (Figure 3.4). In contrast to the pure materials, cross-sectional SEM images of the 30GO sample in Figure 3.5 demonstrate an improved horizontal alignment of the GO sheets. During the formation of the primary film, Na-LgS macromolecules are intercalated between the GO sheets through noncovalent Van der Waals interactions [62]. This arrangement prevents GO sheets from lifting up and losing contact during laser-reduction. After laser-carbonization, unlike the pure components, all of the GO/ Na-LgS composites showed superior morphology leading to higher electrical conductivity.
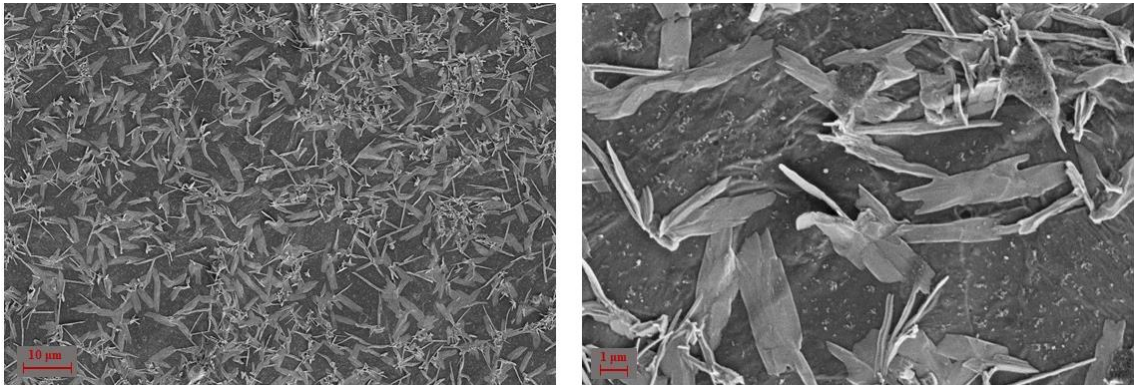


*Figure 3.4  Top view SEM images of the 30GO coated on PET.*
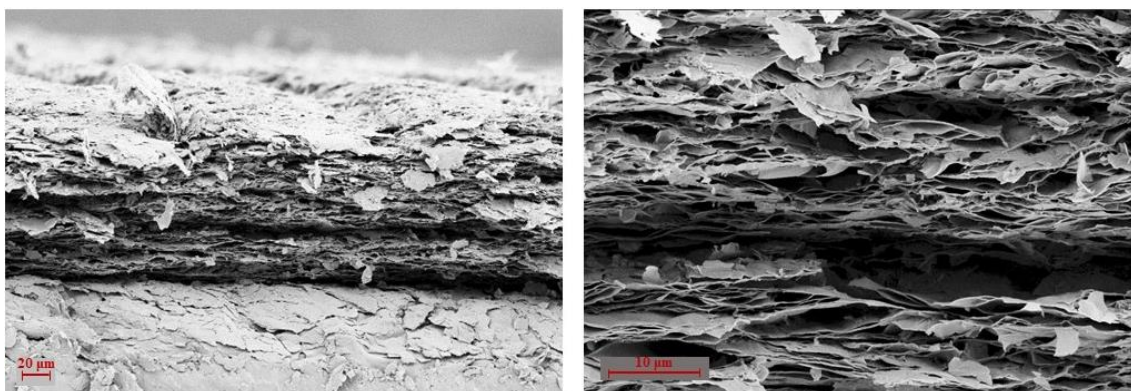
*Figure 3.5  Cross sectional SEM images of the carbonized NaLgS(70)/GO(30).*

## 3.2  Raman Microscopy

Raman spectroscopy was performed to study the level of carbonization of the pure materials and their composition (Figure 3.6 and Figure 3.7). The Raman spectra of the laser-carbonized films show a spectral pattern typically observed in turbostratic carbon materials with three dominant peaks [63]. A D-peak at 1360 cm$^{-1}$ underlining the presence of defects in the graphitic lattice, as well as the G-band ($E_{2g}$ vibration of sp$^2$ carbon atoms) and 2D-band at 1570 cm$^{-1}$ and 2700 cm$^{-1}$, respectively, indicating the second order zone-boundary phonons. While the 2D-band was not observed for unexposed parts of the GO film (Figure 3.6), all the carbonized compositions showed a sharp 2D peak, indicating the presence of stacked layers of graphene. The Raman results suggests that the laser-patterned samples are dominated with sp$^2$ carbon atoms, agreeing with XPS results.

The peak intensity ratio of D- and G-band ($I_D/I_G$) indicates the quality of the formed graphene and the defect density within the graphitic network in the carbonized film. The $I_D/I_G$ ratio for the pure samples and the 30GO composition is shown in Figure 3.6. Surprisingly, although the lowest measured sheet resistance was observed for 30GO (see

section 4.2 for detailed electrical analysis), the sample presents higher $I_D/I_G$ compared to one for carbonized pure Na-LgS. Based on the $I_D/I_G$ analysis, pure Na-LgS show a higher graphitization level and lower defect density compared 30GO or GO. This seemingly counterintuitive effect is attributed to probing the top-layer of the films and the laser-induced carbonization mechanism of the macromolecular Na-LgS primary film. In previous studies it was demonstrated that the upper layers directly exposed to the laser irradiation show a very high degree of carbonization, while in the lower layers the laser energy impact is drastically attenuated [64]. In contrast, the laser-induced reduction of GO follows a mechanism of heat-dissipation across the film [28].
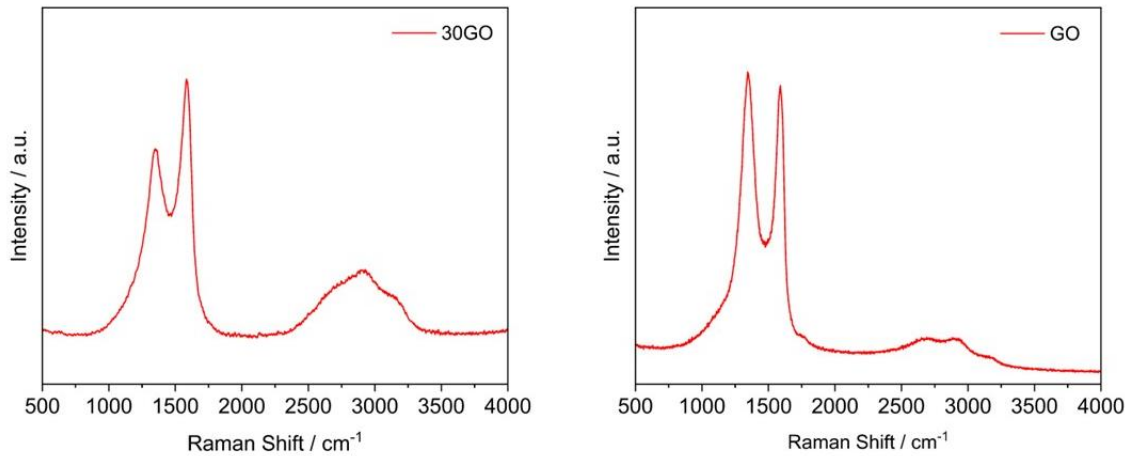


*Figure 3.6  Raman spectra of the uncarbonized (unexposed) GO and 30GO samples.*
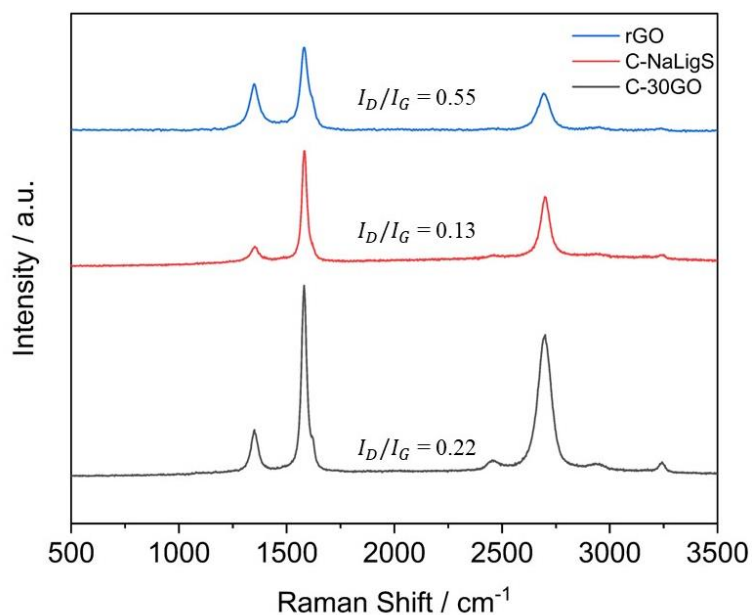
*Figure 3.7  Raman spectra of the carbonized GO, Na-LignS, and 30GO samples.*

## 3.3  X-ray Photoelectron Microscopy (XPS)

X-ray Photoelectron Spectroscopy (XPS) was used to study the chemical composition of the films before and after carbonization. The survey scans indicate sharp peaks of C 1s (284.5 eV) and O 1s (532 eV), as well as Na 1s peaks (1071.9 eV) for the samples consisting of Na-LgS (Figure 3.8) [54]. The chemical composition estimated from XPS data is available on Table 3.1. The NaLgS(70)/GO(30) sample, with the lowest sheet resistance compared to other composition, showed a significant increase in the amount of carbon from 16.7% to 76.4% and decrease in oxygen and sodium from 52.1% and 17.8% to 15.1 and 5.5%, respectively, upon laser carbonization process. This proves the off-gassing happening during the carbonization process. Through this phenomenon, oxygen reacts with carbon to effuse $CO_2$ gas and sodium evaporates due to high instant local temperature. The C 1s XPS spectra can be mainly deconvoluted to four peaks of $sp^2$ carbon

(C=C) at 284.2 eV, $sp^3$ carbon (C-C) at 284.8 eV, C-O at 285.7 eV and C=O at 288.5 eV [45], [49], [54]. XPS results demonstrate the increase of $sp^2$ C=C bonds and decrease of oxygen functional groups upon laser patterning confirming the carbonization occurrence (Figure 3.9 and Figure 3.10).
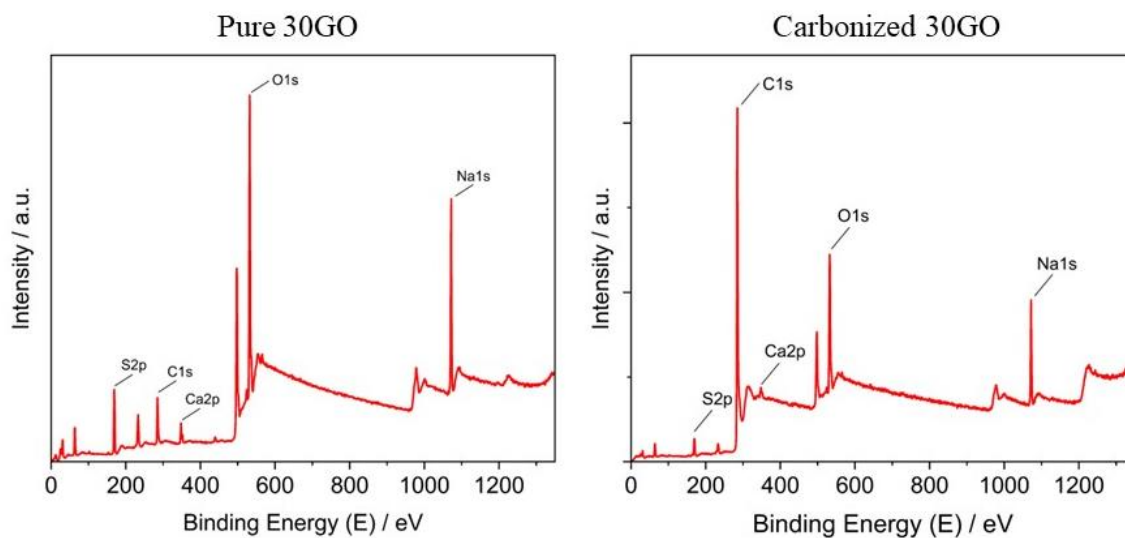


*Figure 3.8 XPS survey of the NaLgS(70)/GO(30) sample before (left) and after (right) carbonization process.*
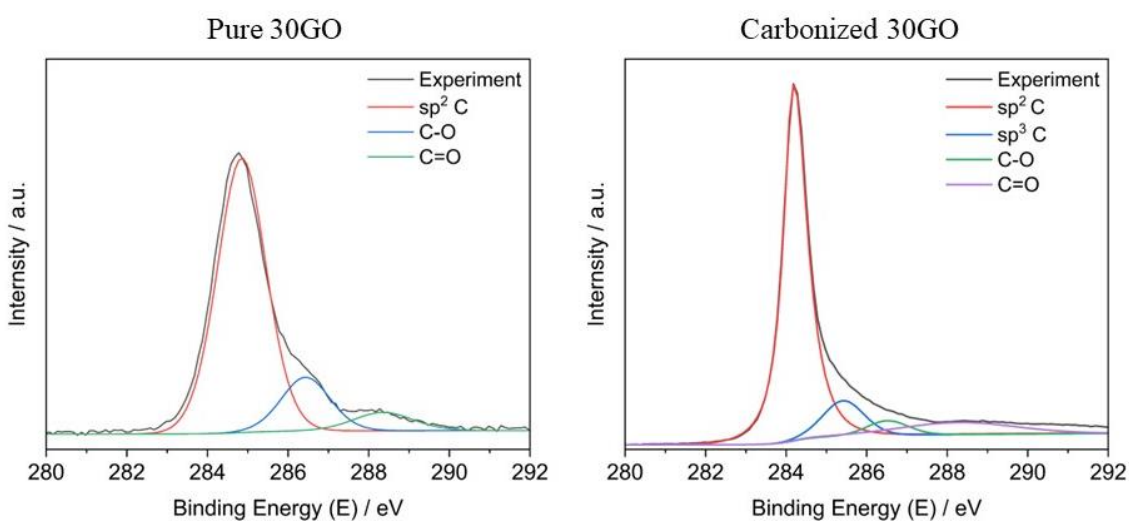
*Figure 3.9  XPS C 1s spectra of the NaLgS(70)/GO(30) sample before (left) and after (right) carbonization process.*
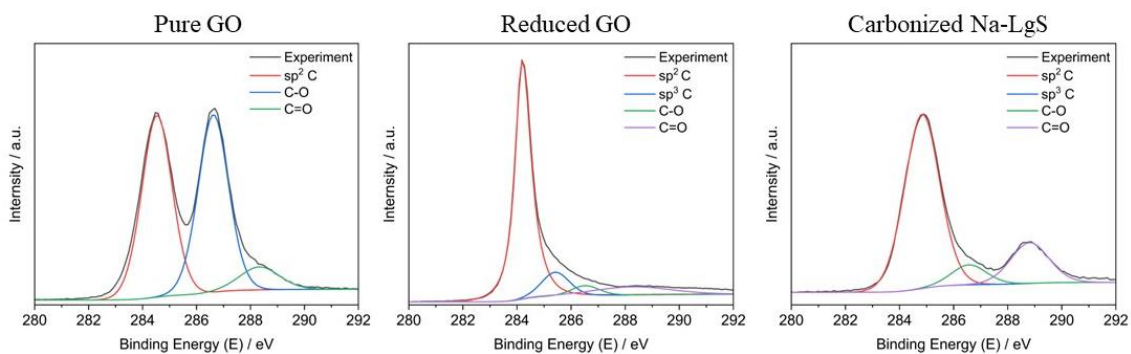


*Figure 3.10  XPS C 1s spectra of the pure GO (left), laser-reduced GO (middle) and carbonized Na-LgS (right).*

*Table 3.1  Chemical Composition of different samples, derived from XPS survey.*

| Peaks | S2p (Rel.At.%) | C1s (Rel.At.%) | Ca2p (Rel.At.%) | O1s (Rel.At.%) | Na1s (Rel.At.%) | C/O |
|---|---|---|---|---|---|---|
| C-Na-LgS | 3.9 | 48.7 | 0.9 | 34.6 | 11.9 | 1.4 |
| rGO | 2.6 | 73.0 | 0.4 | 23.6 | 0.4 | 3.1 |
| GO | 1.2 | 66.6 | 0.2 | 31.8 | 0.2 | 2.1 |
| C-30GO | 2.4 | 76.4 | 0.6 | 15.1 | 5.5 | 5.0 |
| 30GO | 11.6 | 16.7 | 1.8 | 52.1 | 17.8 | 0.3 |

# 4 Electrical Properties of Laser-Carbonized GO/Na-LgS

In this chapter, electrical properties of the carbonized samples are measured and analyzed. In this regard, four-point probe measurement, which was used to measure the sheet resistance of the carbonized parts, is described in this chapter. Then, the sheet resistance is optimized based on the various laser powers and speeds using contour plot visualization. After optimizing the process with respect to laser parameters and material composition, a bending-resistance test is carried out to validate the flexibility of the film for flexible electronics applications.

## 4.1 Introduction to Sheet Resistance

Sheet resistance is used for two-dimensional systems that include thin films as two-dimensional entities. The regular resistance for a 3D geometry can be written as

(Eq. 4.1)
$$R = \rho \frac{L}{A} = \rho \frac{L}{Wt}$$

Where $\rho$ is the material resistivity (dependent on material, not geometry), $A$ is the cross-section area, and $L$ is the length. $W$ is the width and $t$ is the thickness.

If the sheet resistance ($R_s$) is defined as resistivity per thickness, then the resistance can be written as

(Eq. 4.2)
$$R = R_s \frac{L}{W}$$

Sheet resistance is a subset of resistivity that applies to homogeneous sheet thickness with a commonly known unit of $\Omega/\square$ (ohms per square). Sheet resistance can be interpreted as the resistance of a square unit of the film. On the other hand, as long as the width and length of the measured area are equal (W = L), the sheet resistance is equal to regular resistance ($R = R_s$).

The sheet resistance can be measured using two popular methods of two-point and four-point probe measurements. Four-point probe instrument is shown in Figure 4. In four-point probe measurement, in contrast to conventional two-point resistance measurement, one pair of probes injects the current while the other pair measures the voltage. Since no current flows in the sensing probe, the device measures the voltage developed across the resistance, followed by eliminating errors caused by test lead and contact resistance.
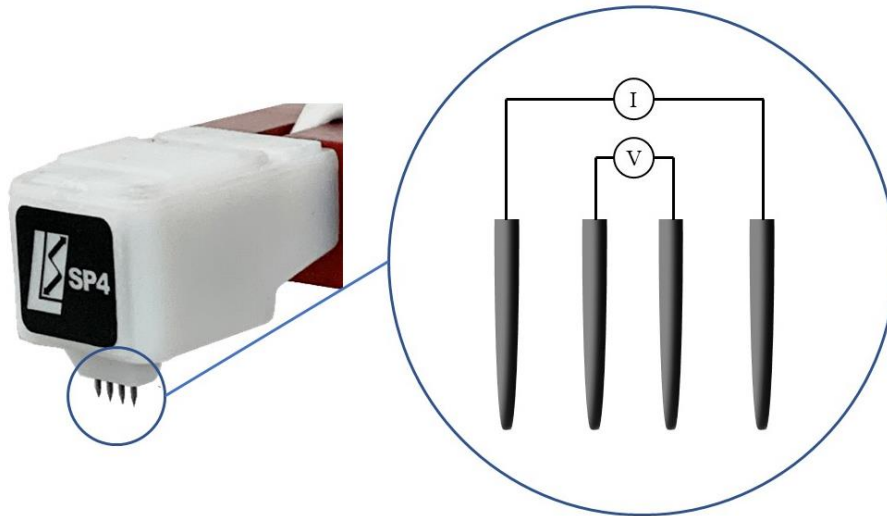
*Figure 4.1 Four-point probe device and working diagram, in which one pair creates a current in the material while the other pair measures the voltage.*

Equation 4.2 can be used to measure the sheet resistance of a film using a two-point probe. This method measures the resistance between two ends of the sample (R in the equation). By knowing the width (W) and length (L) of the measurement area, the sheet resistance can be calculated using Equation 4.2.

A Digital Multimeter (DMM) is used to generate the current and measure the voltage resulting in a V-I plot. It is proved by Smits [65] that for film thickness less than half of probe spacing and lateral dimensions 40 times greater than the probe spacing, the V-I should be a linear plot with the slope of $\frac{\ln(2)}{\pi} R_s$, where $\frac{\ln(2)}{\pi} = 4.53$. As a result, the sheet resistance is determined from the slop of measured voltage versus the injected current plot.

## 4.2  Laser Carbonization Process Optimization

To investigate the electrical conductivities of the laser-patterned GO/Na-LgS composite materials, films with an average thickness of 20 μm were prepared and laser-treated. A range of different laser parameters (i.e., incident laser power and scanning speed) were tested to pattern sample lines (10×1 mm) on the primary films for sheet resistance measurement. Contour plots showing sheet resistance (measured by a four-point probe) as a function of power and speed are shown in Figure 4.2. Dark blue spots indicate the lower sheet resistance, while red spots show higher sheet resistance. The white regions indicate the inapplicable laser parameters where either too high energy densities (low speed and high power) destroy the primary film and evaporate the materials from the film's top surface, or the laser energy density is insufficient to induce carbonization.
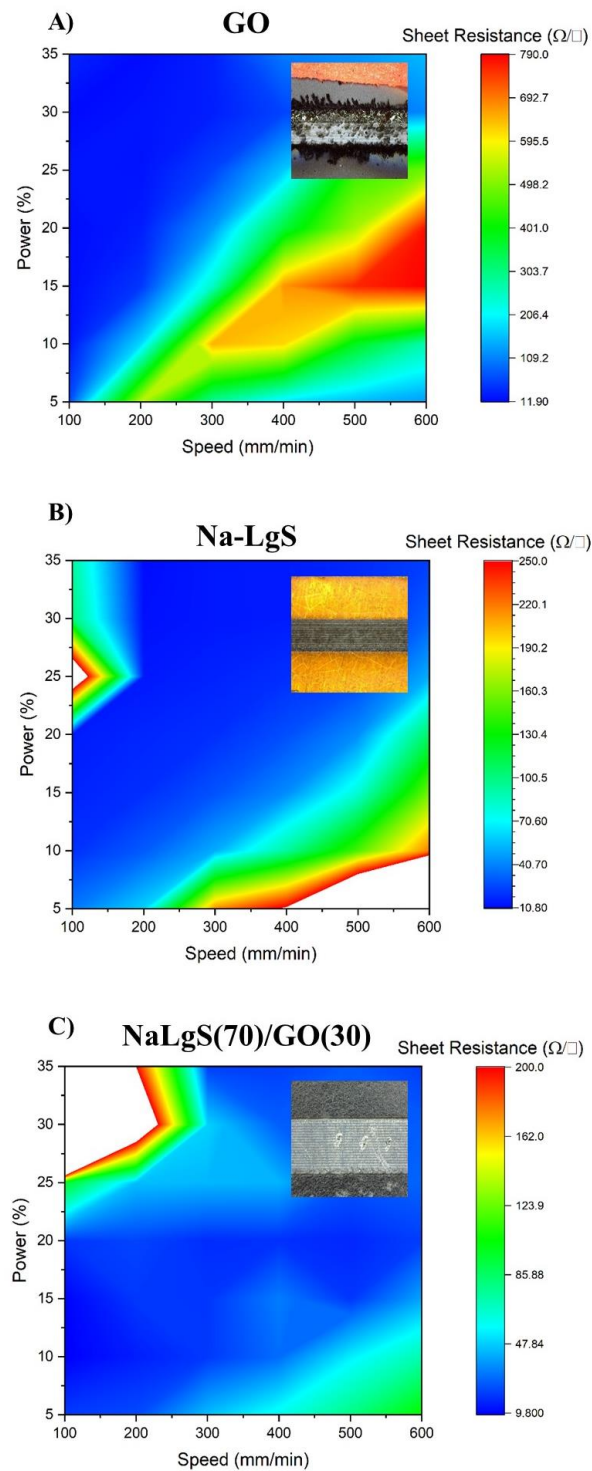
*Figure 4.2  Contour plot of sheet resistance for A) GO, B) Na-LgS, and C) 30GO samples. The insets are optical images of the carbonized lines. For the speeds lower than 100 mm/min and powers higher than 35% is the laser carbonization is inapplicable due to significant ablation of the carbon substrate*

It is observed that for pure GO the lowest sheet resistance (16.2 Ω/□) occurs at high energy spots where the speed is low (<10 mm/min) and power is high (~10%), while the lowest sheet resistance for pure Na-LgS (11.9 Ω/□) is achievable at lower laser powers (Power 30% and Speed 100 mm/min). Nevertheless, the 30GO sample shows moderate required energy to provide the highest conductivity, whereas the very high (S<250 mm/min and P>25%) and low energies (S>400 and P<10%) are insufficient for useful carbonization. As shown, the optimized laser parameters for the lowest obtainable sheet resistance heavily depend on the material and composition. Therefore, we carried out the same optimization process using the contour plot approach for all sample compositions to increase the statistical value of our analysis. The lowest sheet resistances obtained for each composition at optimized laser parameters are summarized in Table 4.1.

Table 4.1  Quantitative laser parameters and electrical conductivity for various GO/Na-Ligns compositions (60 GO = 60 wt% GO, 40 wt% Na-Ligns).

| Sample | Average Film Thickness (μm) | Power (%) | Speed (mm/min) | Sheet Resistance (Ω/□) | Conductivity (σ/cm) |
|--------|------------------------------|-----------|----------------|-------------------------|----------------------|
| GO | 21.6 ± 1.1 | 5 | 80 | 26.8 | 17.27 |
| | | | 100 | 39.4 | 11.75 |
| | | | 150 | 240 | 1.92 |
| | | 10 | 80 | 16.2 | 28.57 |
| | | | 10 | 19.5 | 23.74 |
| | | | 150 | 34.2 | 13.53 |

| | | | | | |
|---|---|---|---|---|---|
| | | | 80 | 17.4 | 25.77 |
| | | 5 | 100 | 24.1 | 18.60 |
| | | | 150 | 46.3 | 9.68 |
| **60GO** | 22.3 ± 1.2 | | 80 | 23.2 | 19.32 |
| | | 10 | 10 | 19.7 | 22.76 |
| | | | 150 | 21.1 | 21.25 |
| | | | 80 | 19.1 | 24.58 |
| | | 5 | 100 | 17 | 27.61 |
| | | | 150 | 27.4 | 17.13 |
| **50GO** | 21.3 ± 3.1 | | 80 | 23.6 | 19.89 |
| | | 10 | 10 | 17.5 | 26.80 |
| | | | 150 | 14.4 | 32.60 |
| | | | 80 | 18.2 | 16.80 |
| | | 5 | 100 | 28.6 | 10.69 |
| | | | 150 | 47.4 | 6.45 |
| **40GO** | 32.7 ± 3.5 | | 80 | 26 | 11.76 |
| | | 10 | 10 | 21 | 14.56 |
| | | | 150 | 21.5 | 14.22 |
| | | | 80 | 11.3 | 40.9 |
| | | 5 | 100 | 8.9 | 52 |
| | | | 150 | 10.5 | 44.12 |
| **30GO** | 21.6 ± 2.3 | | 80 | 12.4 | 37.31 |
| | | 10 | 10 | 9.8 | 47.20 |
| | | | 150 | 11.6 | 39.92 |

Among all GO/Na-LgS compositions, 30GO, which stands for 30% GO and 70% Na-LgS, shows the lowest sheet resistance of 8.9 $\Omega/\square$ obtained with laser power and speed of 10% and 100 mm/min (P10-S100), while sheet resistances of 10.8 (P35-S200) and 11.9 $\Omega/\square$ (P30-S100) are obtained for pure GO and Na-LgS, respectively. Figure 4.3 represents the sheet resistance of different GO/Na-LgS composites for constant laser parameters. Obviously, by increasing the laser scanning speed, meaning decreasing the laser energy, the sheet resistance of each sample increases. However, a dropping trend is observed for certain laser parameters except for the 40GO sample. Despite the fact that 30GO shows the lowest sheet resistance, 20GO is hardly coated on the PET due to the intrinsic adhesive property of Na-LgS when combined with GO. In fact, the 20GO precursor sticks to the blade while coating followed by leaving a thin wet coating behind. Moreover, when increasing the Na-LgS portion further, the mechanical stability upon bending of the laser-carbonized materials is affected.

## 4.3  Bending

A specially designed movable electrode stage was implemented to study the electrical performance of the laser-carbonized films upon bending, which is a crucial attribute for transient/flexible electronics. As shown in Figure 4.4A, a laser-carbonized strip (10 × 1 mm) on a flexible PET substrate is mounted between two electrode clips (one movable) while the end-to-end resistance is monitored upon quantitative periodic bending. One electrode moves toward the other with a predefined speed of 10 $\mu m \cdot s^{-1}$ to constantly bend the straight strip to the maximum curvature of 0.28 $mm^{-1}$. Figure 4.4B shows an increase in the resistance upon bending to different curvatures. At curvatures > 0.28 $mm^{-1}$, an

indefinite change in resistance is observed. This is attributed to the emergence of fractures and micro-cracks in the positive bending position [64]. Nevertheless, these cracks are recovered after stretching back to the initial position, followed by retaining the electrical integrity of the material.
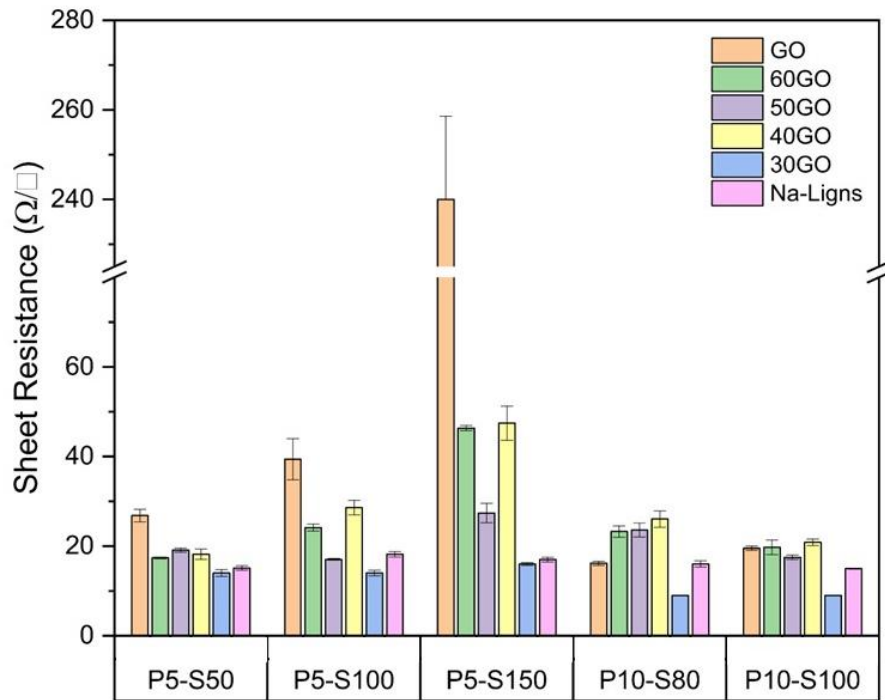


*Figure 4.3  Bar chart indicating various samples lowest sheet resistance for different laser power and speed. P5S50 means 5% power and 50 mm/min laser nozzle movement speed.*
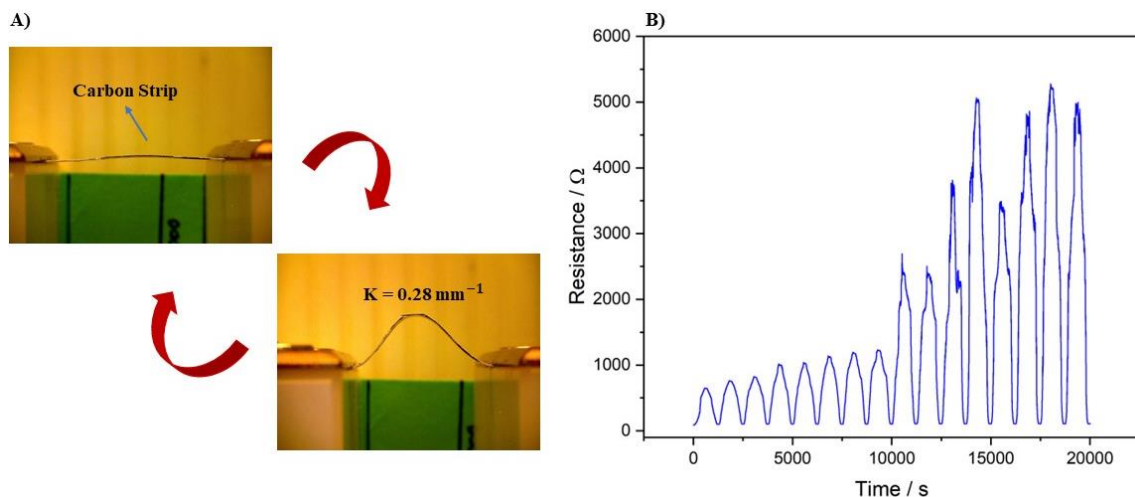
*Figure 4.4  A) Photographs of sample strip fixed between movable electronics showing the cyclic bending loading. B) Measured resistance of the sample over repetitive bending.*

## 4.4    Comparing the Sheet Resistance with Literature

Numerous research has been done regarding laser carbonization of various organic, polymeric, and bio-based materials [66]–[68]. Laser carbonization, which sometimes referred as laser graphitization, has been proved to be a fast, accurate, flexible, and controllable method for carbonizing materials compared to other carbonization methods such as thermal and chemical [69]. Despite all the superiorities, the obtained level of carbonization and electrical properties are highly dependent on the type of laser and its parameters, precursor, and environmental conditions. Due of this complexity, there are several challenges to achieving high electrical conductivity. To address this challenge and obtain a high electrical conductivity, researchers have implemented either expensive and complex materials like gold coating [45], or complex laser environments such as gas-filled chamber [70]. In comparison with the high-cited works showed in Figure 4.5, this work

41

stands among the lowest sheet resistances while maintaining the simplicity of material and

fabrication method.
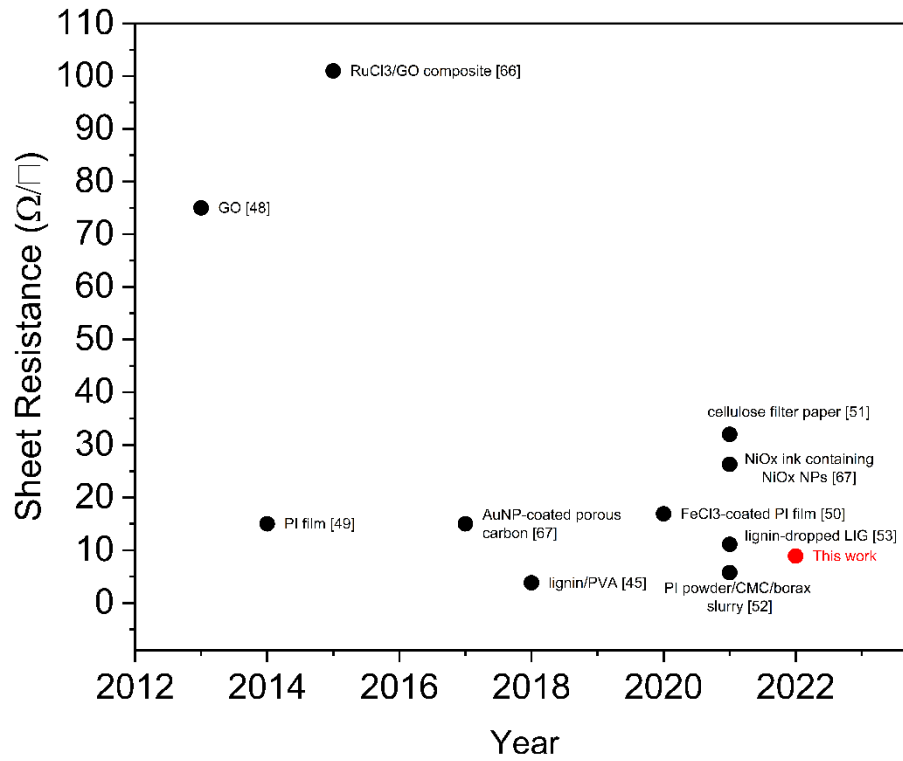


*Figure 4.5  Comparing sheet resistance achieved in this work with literature.*

# 5 Laser-Scribed Transient Radio Frequency Identification (RFID) Antenna

In this Chapter, an application for the laser carbonized films is provided. First, through a brief introduction, the applicability of the material and method is examined for RFID fabrication. Then, the process is further explained by introducing fabrication process of an RFID tag. The RFID tag is tested using an RFID reader to activate an LED via contactless voltage induction. Since the tag is made by eco-friendly and water-soluble materials, the disintegration performance of the tag in water is examined in the end of this chapter.

## 5.1 Introduction

The recently proven concept of transient electronics opens a new opportunity for the next generation of electronics that can undertake a pre-programmed demolition. Such ability is appropriate for a broad field of electronics to reduce e-waste. Although graphene-based electronics are not being designed for this purpose, they may benefit in this arena due to the affinity of the base material (GO) to be dispersed in water. The design freedom brought about by laser patterning and the ability to accurately print 70 µm-width lines on carbon-based films (Figure 5.1), allow for fabricating complex and accurate electronic patterns.
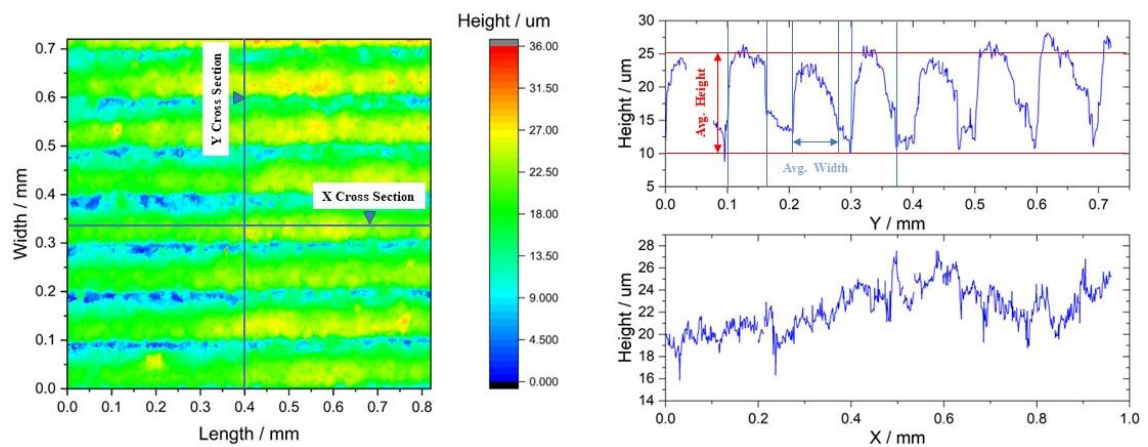


*Figure 5.1 (Left) Surface profile plot of the laser scribed sample showing the laser line footprint and (right) quantified height associated with the X and Y cross sections shown on the contour plot.*

## 5.2 RFID Working Principle

An RFID tag, also known as a transponder, is a tiny device that may be attached to an object to identify and track it. A microchip, an antenna, and a substrate or encapsulating material comprise the sub-systems within a tag. The microchip stores data, while the antenna sends and receives data. RFID tags can be categorized as passive and active based

on the power source. Active tags require a battery to power up the integrated chip (IC), while passive tags use the voltage induced by an electromagnetic field flux generated by the reader. An RFID system consists of a tag and a reader. The reader creates and sends an interrogation signal to the tag. The reader powers a passive tag through magnetic induction (near-field coupling) and electromagnetic wave capture (Figure 5.2).
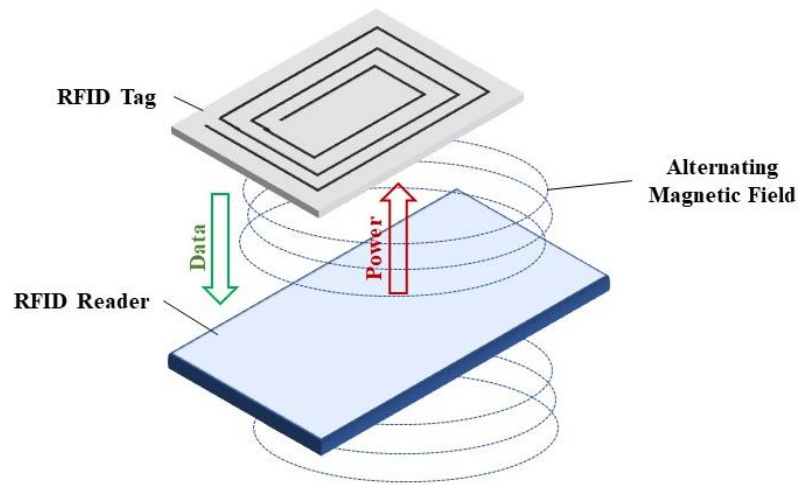


*Figure 5.2  Schematics of RFID system communication consisting of an RFID tag and RFID reader.*

According to Faraday's law, a time-varying magnetic field passing over a surface bordered by a closed route induces a voltage around the loop. When the tag and reader are near together, the time-varying magnetic field ($B$) produced by a reader antenna coil induces a voltage with the same frequency in the closed tag antenna coin. The generated voltage in the coil causes a current to flow through it. The induced voltage on the tag antenna coil equals the magnetic flux's temporal rate of change ($\psi$). Equation 5.1 shows the induced voltage, where $N$ is the number of coil's turns.

$$\text{(Eq. 5.1)} \qquad\qquad\qquad V_0 = -N \frac{d\psi}{dt}$$

The generated magnetic field caused by current (*I*) flowing in reader coil would be *B,* with

the expressions for both being as follows.

$$\text{(Eq. 5.2)} \qquad\qquad\qquad I = I_0 \sin(wt)$$

$$\text{(Eq. 5.3)} \qquad\qquad\qquad B = B_0 \sin(wt)$$

Then, the voltage induced in tag coil is:

$$\text{(Eq. 5.4)} \qquad\qquad\qquad V = V_0 \sin(wt)$$

## 5.3 RFID Geometry Optimization Based on the Inductance and Resistance

The ratio of the magnetic flux created by a current carrying conductor to the current

travelling through it reflects its self-inductance, as shown in Equation 5.5. In this equation,

$\Phi$ is the magnetic flux (Weber) and $i$ is the current (Amp).

$$\text{(Eq. 5.5)} \qquad\qquad\qquad L = \frac{\Phi(i)}{i}$$

Several equations have been proposed to estimate the inductance in a coil spiral [71], [72].

The Equation 5.6 is adopted from [73] to approximate the L for a square coil shown in

Figure 5.3.

$$\text{(Eq. 5.6)} \qquad\qquad L = \frac{1.27 \, \mu \, n^2 \, d_{avg}}{2} \left[\ln\left(\frac{2.07}{\varphi}\right) + 0.18\varphi + 0.13\varphi^2\right]$$

In this Equations, $n$ is the number of turns, $d_o$ and $d_i$ are the outer and inner diameters of the coil, as is shown in the Figure 5.3. $d_{avg}$ is the average of the inner and outer diameters $((d_o + d_i)/2)$ and $\varphi$ is the fill factor with the following formula.

(Eq. 5.7) $$\varphi = \frac{d_o - d_i}{d_o + d_i}$$

To find out the end-to-end resistance of the square coil RFID antenna, the total length of the conductance trace $l_c$ should be known as a function of the coil geometry which is as follows.

(Eq. 5.8) $$l_c = 4nd_o - 4nw - (2n + 1)^2(s + w)$$

By substituting the Equation 5.8 to Equation 4.2, the end-to-end resistance will be as follows.

(Eq. 5.9) $$R = R_S \frac{l_c}{w}$$
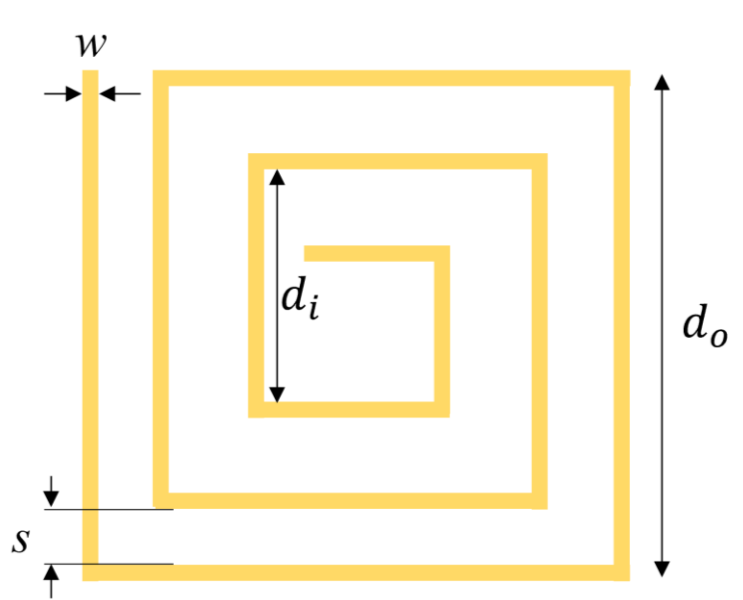


*Figure 5.3  Square coil geometry.*

According to Equation 5.6, the inductance increases by an increasing the number of turns, which is ideal for improving the coil performance. However, as is obvious from Equation 5.8 and 5.9, the end-to-end resistance of the coil also increases by an increase in the number of turns. In order to enhance the current generated by the induced voltage in the coil, the resistance should be kept as low as possible. In this regard, a basic optimization technique was used to discover the ideal number of turns. In this regard, a MATLAB code (see the Appendix section) calculates and plots the inductance and conductivity (1/R) as a function of number of coil's turns, respectively. The two curves intersect nearly at n = 5.5 as the optimum point, as illustrated in Figure 5.4. However, since the number of turns should be an integer and higher conductivity is preferred, the number of turns was set as five.
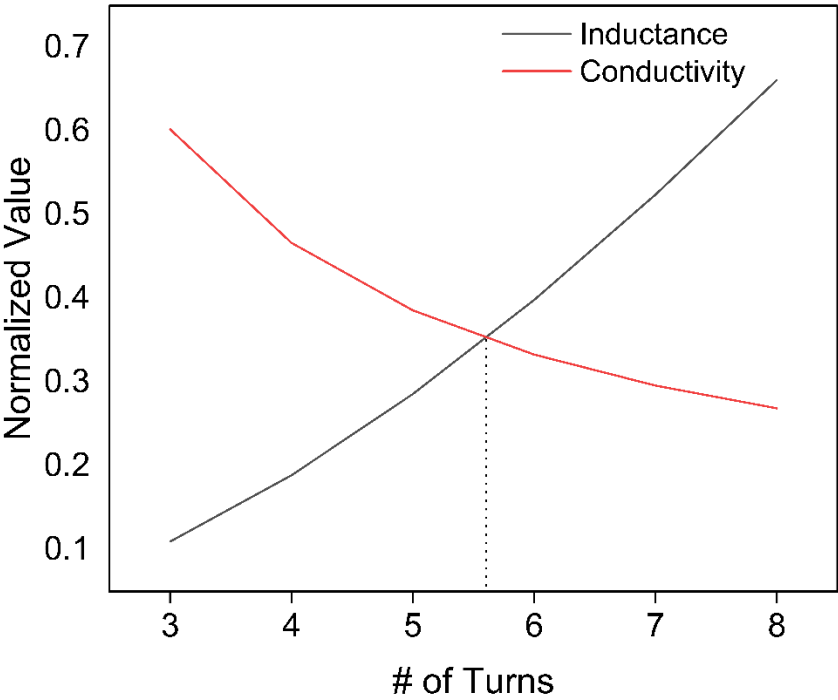


*Figure 5.4 Optimization of number of coil's turns based on inductance and conductivity.*

## 5.4 RFID Proof-of-Concept

Having optimized the electrical properties and geometry, an RFID antenna tag was fabricated. In this regard, the material with lower sheet resistance (30% GO and 70% Na-LgS) was coated on a PET substrate. The same laser parameters (10 % power and 10 mm/min speed) were used to fabricate the laser-scribed square coil RFID. An image of a laser-patterned coil-shaped RFID antenna is shown in Figure 5.5. The tag is $50 \times 50$ mm and has five turns with one mm-width line.
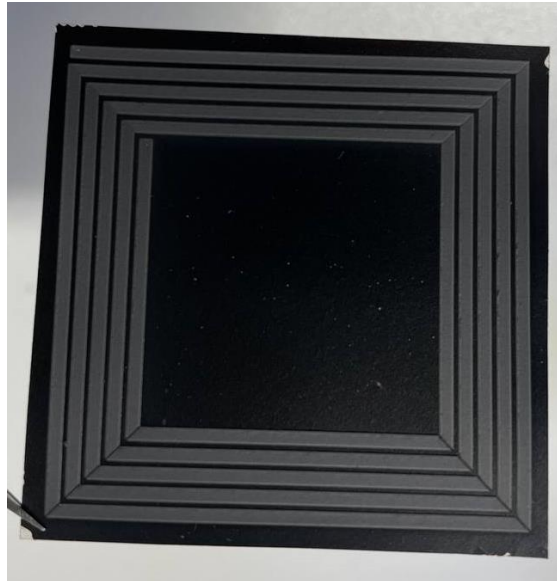


*Figure 5.5  Optical image of the 5-turn laser-scribed RFID tag with an LED attached end-to-end.*

Figures 5.6 and 5.7 show the applicability of the RFID antenna. Briefly, a reader (white item) generates a specific magnetic field, which induces a current in the RFID antenna. The induced current powers an integrated chip (IC) to build a wireless data transfer communication with the reader in a real RFID tag.

To validate the occurrence of the contactless induction and functionality of the fabricated RFID antenna, an LED was attached to the two ends of the antenna while the assembly was exposed to a commercial RFID reader. A gradual on/off switching of the LED was observed with a horizontal and vertical movement of the antenna toward the center of the reader where maximum electromagnetic flux occurs. The zoomed-in image in Figure 5.7 illustrates the existence of contactless induction, considering that the LED is on despite the prominent visible gap between the antenna and reader.
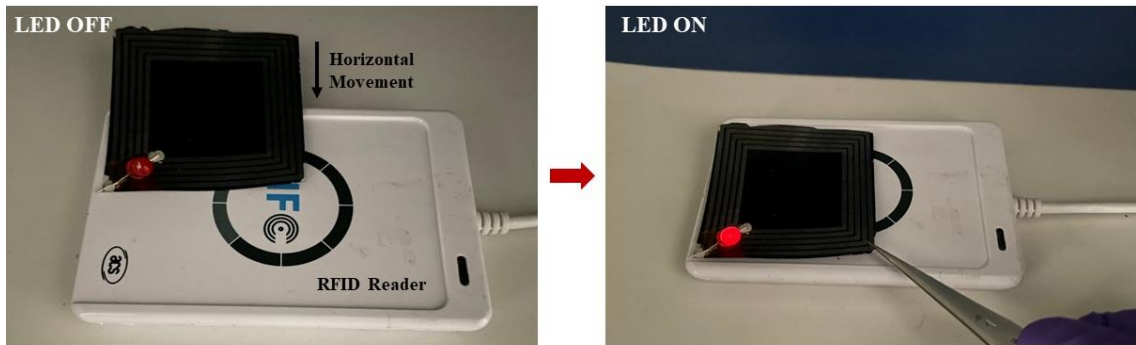


*Figure 5.6  Optical image of the horizontal movement of the tag toward the center of the RFID reader where the maximum electromagnetic flux occurs making the LED turns on.*
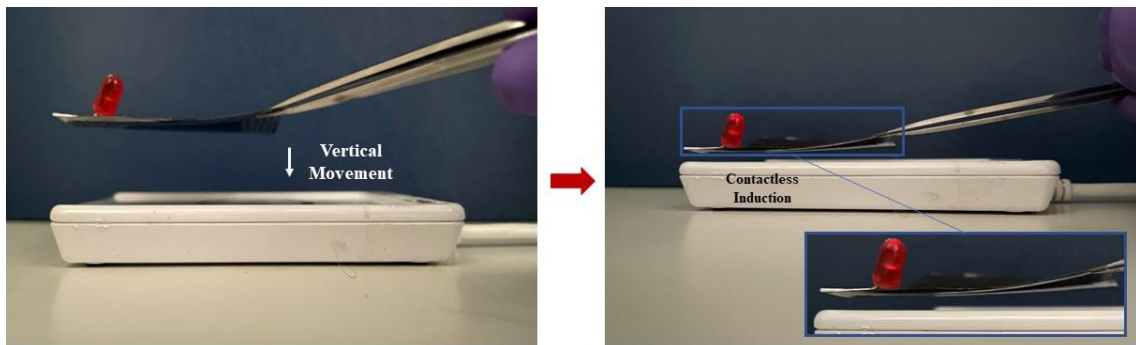


*Figure 5.7 Optical image of the Vertical movement of the tag toward the surface of the RFID reader where the maximum electromagnetic flux occurs making the LED turns on. The inset shows the gap between the tag and the reader.*

## 5.5 Transient Property

To demonstrate the transient and recycling properties of the films, an RFID tag patterned on PET was immersed into distilled water at room temperature under turbulent conditions (120 rpm) as shown in Figure 5.8(A, B). As discussed above, due to the inherent hydrophilicity of the primary materials (GO and Na-LgS) the unexposed, non-carbonized parts of the film are easily dispersed in water while the carbonized regions (coil-shaped RFID) stick to the substrate. However, while transferring into the water, unexposed parts partially drag the carbonized parts into the aqueous phase due to some structural connection with the unexposed parts of the film. As shown in Figure 5.8D-G, the color of the water starts changing to brown after two minutes because of dispersion of both the GO and Na-LgS. After almost ten minutes, when all material is disintegrated from the PET substrate, the PET substrate and the remaining material in water can be easily extracted for recycling (Figure 5.8C). It is noteworthy to say that all samples tested in this study were capable of disintegration in a similar manner.

With a high extinction coefficient at the laser beam's wavelength, the primary film material composition absorbs most of the laser's energy, preventing the substrate from melting and intermixing with the coated film (Figure 5.9A). As demonstrated in the optical cross-sectional images in Figure 5.9B, there is a narrow gap between the PET substrate and the primary film before and after laser-carbonization. The resulting weaker adhesion between the substrate and the film allows the carbonized parts to be separated from the substrate. This process happens due to the tension caused by the separation of nearby unexposed materials and agitation (turbulence) in the water.

Graphene-based nanomaterials (GFN) can infiltrate the environment throughout the manufacturing, use, and end-of-life stages. Following that, discarded graohene undergos a variety of changes in the air, terrestrial, and aquatic environment. The effect of the material on the environment is highly dependent on the environment and its concentration. As a result, by controlling the environment and the concentration, graphene can be considered environmentally friendly [74].
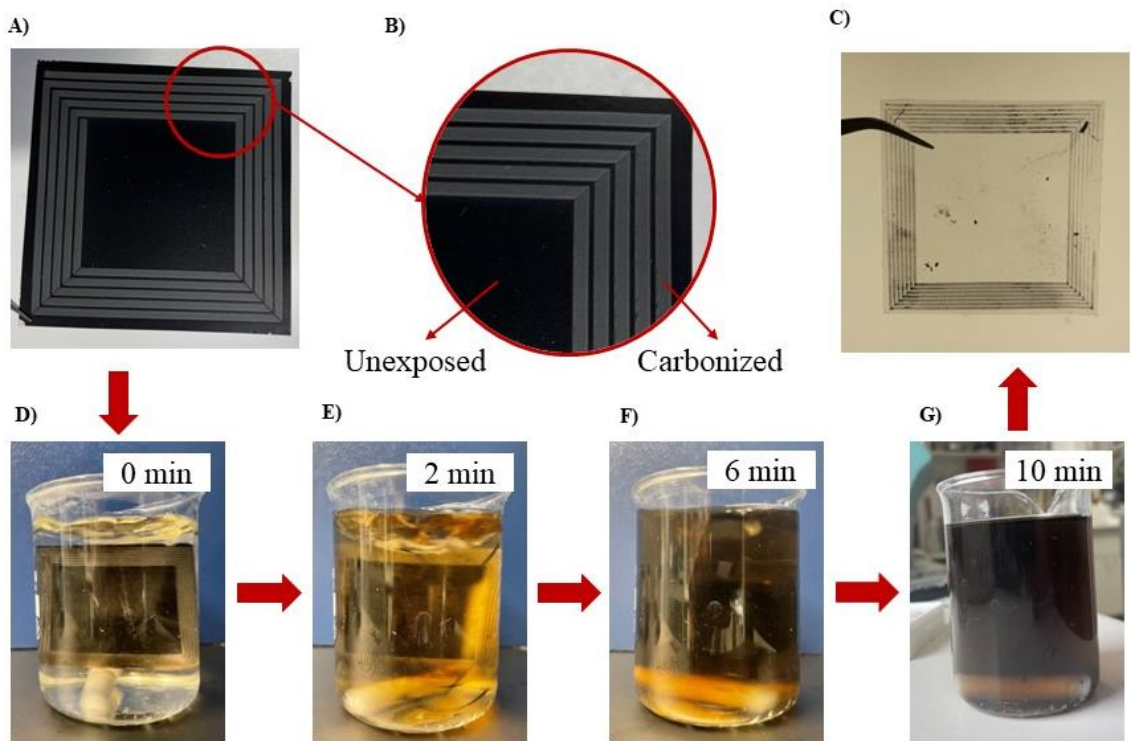


*Figure 5.8 A, B) Photographs of the laser-patterned RFID antenna tag. The tag is 5*5 cm. C) Remaining PET substrate ready for recycling. D-G) RFID tag dissolution steps.*
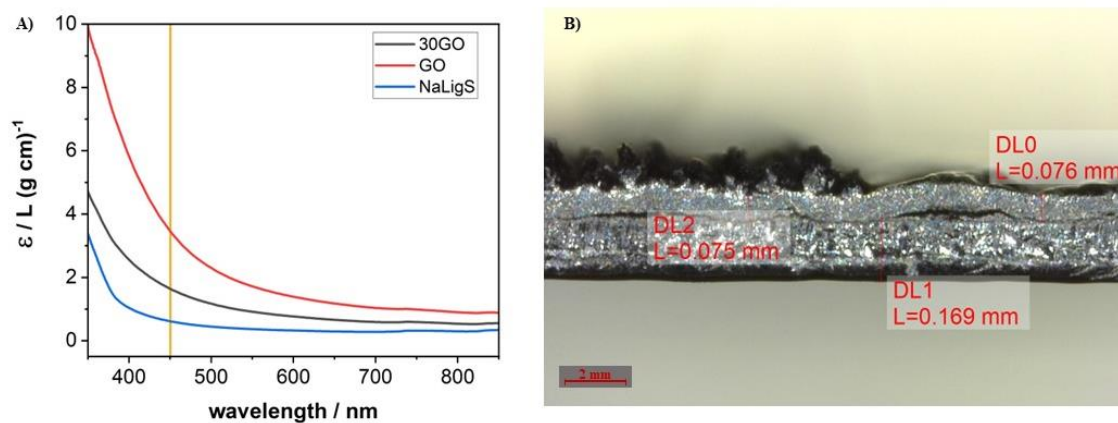
*Figure 5.9  A) Extinction coefficient of the pure materials and the composition, B) Cross sectional optical microscopy image of the GO sample. A narrow separation line between the material and the substrate is obvious.*

# 6  Conclusion and Future Work

In this work, transient circuits with significant mechanical and electrical properties were designed and fabricated. To aim this, different compositions of Sodium Lignosulfonate (Na-LgS) and Graphene Oxide (GO) were coated on PET substrates to prepare the primary films. Laser beam with a range of powers and speeds were used to carbonize thin films. The sheet resistance for carbonized samples with various compositions and laser parameters were measured. The precursor made of 30% GO and 70% Na-LgS (30GO) showed the lowest sheet resistance (8.9 $\Omega/\square$) among all samples. To examine the mechanical flexibility of the sample for flexible electronics potential application, the electrical resistance of a string of the sample was tested under cyclic bending loading. Although the sample tend to show high resistance at the highest curvature after nine bending loadings, the electrical resistance was able to be recovered after returning to the initial position.

SEM, XPS, and Raman spectroscopy were employed to study morphology and chemical composition of the carbonized films. The sample made of 30% GO and 70% Na-LgS experienced a higher level of carbonization under 10% power and 100 mm/min laser power and speed. An RFID tag with optimized geometry was designed and fabricated. As a proof-of-concept, the fabricated tag showed the ability to light on an LED using contactless voltage induction sourced from an RFID reader. In the end, the transient property of the circuit was proved by dissolving the tag in water over time.

Typical RFID tags are made of PET substrate, metal circuit, and a paper cover. Each of these individual materials is highly efficient and recyclable when separately entering the

54

recycling process. However, RFID tags are considered unrecyclable since the integrated materials are not separable during the so-called "sorting" process, where different categories of materials are separated. The commercially inviable process of separating materials is attributed to the low thickness and adhesiveness of laminated layers.

Considering the bio-derived, carbon-based nature of the materials used to fabricate the circuits in this study, their transient character may be implemented into a real device to create environmentally benign single or few-use electronics. For example, single-use train tickets are being used in public transport systems across the globe (e.g. Toronto, Amsterdam etc.). Figure 6.1 shows that these tags are typically made of often non-ecofriendly metal circuits and chemical-based plastic covers. In such single-use applications, tags are often discarded and pollute the environment, while their time-consuming and costly disassembling process limits their recyclability. Nevertheless, considering the benefits of integrating water-soluble, biocompatible RFID tags, a huge amount of waste will be reduced while maintaining the overall cost.



*Figure 6.1  Transportation tickets with an integrated RFID antenna tag made of various materials.*

Commercial applications for this research will be single-use and few-use electronic devices that are reliant on RFID technologies, such as but not limited to transit/event tickets, packaging and sensors industry. The advantages of our invention compared to other methods include (1) facile processing with comparable electrical and mechanical properties, (2) production shape freedom, (3) reproducibility, (4) scalability and mass production, (5) environmentally friendly, and (6) cost-effective. To conclude, by developing our final product, substantial reductions in e-wastes pollution can be realized.

Based on the experimental data, literature review, and market research, the following paths are recommended.

- Further improvement of electrical conductivity: although one of the highest electrical conductivities was achieved compared to literature, it is still far lower than metals – e.g., aluminum electrical conductivity is $3.5 \times 10^5$ S cm$^{-1}$ while our work is $6.6 \times 10^1$ S cm$^{-1}$. This path could be achievable by using nanofillers, such as carbon nanodots.

- According to literature, it is very challenging to achieve very high electrical conductivities in laser carbonized films. This could be attributed to either the defects emerged during the process, or the limitation in thickness of films. As a result, one possible approach could be investigation of application with relatively high sheet resistance, i.e., 10 $\Omega/\square$. One recommendation in this regard is transient micro circuits.

- Graphene Oxide, which is quite an expensive material (~$50/g), can be replaced with other materials to undergo the same performance in terms of electrical and mechanical properties. Possible options could be cellulous or PVA [45].

- The PET substrate, which currently is not transient and must still be recovered, can be replaced with a substrate with transient properties, such as Polyvinyl alcohol (PVA) or enzyme-based substrates [75].

# Appendix - Optimization MATLAB Code

```matlab
clc; clear;

% defining the parameters
mue = 4e-7 * pi; % air permeability
pi = 3.14;
n = [3, 4, 5, 6, 7, 8]; % number of turns
do = 50; % outer diameter
w = 1; % conductance trace
s= 0.4; % gap
di = do - 2*w.*n - s.*(2*n-2); % inner diameter

dav = (do + di)/2; % average diameter
phi = (do - di)/(do + di); % parameter phi

% calculating the inductance
L = ((1.27 * mue * n.^2 .* dav)/2) .* (log(2.07/phi) + 0.18 *
phi + 0.13*phi^2);
L = L./ norm(L);
plot(n, L)
hold on

% calculating the Conductivity
lc = 4*n*(do - w) - ((2*n+1).^2)*(s+w); % coil total length
R = 9 * (lc./w); % resistance
si = 1./R; % conductivity
si = si./ norm(si);
plot (n, si)
```

# References

[1]  C. P. Baldé, V. Forti, V. Gray, R. Kuehr, and P. Stegmann, *The global e-waste monitor 2017: Quantities, flows and resources*. United Nations University, International Telecommunication Union, and …, 2017.

[2]  P. Agreement, "Paris agreement," in *Report of the Conference of the Parties to the United Nations Framework Convention on Climate Change (21st Session, 2015: Paris). Retrived December*, 2015, vol. 4, p. 2017.

[3]  A. Kumar, M. Holuszko, and D. C. R. Espinosa, "E-waste: An overview on generation, collection, legislation and recycling practices," *Resour. Conserv. Recycl.*, vol. 122, pp. 32–42, Jul. 2017, doi: 10.1016/J.RESCONREC.2017.01.018.

[4]  J. S. Shim, J. A. Rogers, and S. K. Kang, "Physically transient electronic materials and devices," *Mater. Sci. Eng. R Reports*, vol. 145, p. 100624, Jul. 2021, doi: 10.1016/J.MSER.2021.100624.

[5]  S. W. Hwang *et al.*, "A physically transient form of silicon electronics," *Science*, vol. 337, no. 6102, pp. 1640–1644, Sep. 2012, doi: 10.1126/SCIENCE.1226325.

[6]  L. A. Wehner, N. Mittal, T. Liu, and M. Niederberger, "Multifunctional Batteries: Flexible, Transient, andTransparent," *ACS Cent. Sci.*, vol. 7, no. 2, p. 231, Feb. 2021, doi: 10.1021/ACSCENTSCI.0C01318.

[7]  Y. Chen *et al.*, "Transient Light Emitting Devices Based on Soluble Polymer Composites," *Sci. Reports 2018 81*, vol. 8, no. 1, pp. 1–6, Apr. 2018, doi: 10.1038/s41598-018-24816-y.

[8]  C. J. Bettinger and Z. Bao, "Organic Thin-Film Transistors Fabricated on Resorbable Biomaterial Substrates," *Adv. Mater.*, vol. 22, no. 5, pp. 651–655, Feb. 2010, doi: 10.1002/ADMA.200902322.

[9]  S. W. Hwang *et al.*, "Biodegradable elastomers and silicon nanomembranes/nanoribbons for stretchable, transient electronics, and biosensors," *Nano Lett.*, vol. 15, no. 5, pp. 2801–2808, May 2015, doi: 10.1021/NL503997M.

[10]  R. Feiner, S. Fleischer, A. Shapira, O. Kalish, and T. Dvir, "Multifunctional degradable electronic scaffolds for cardiac tissue engineering," *J. Control. Release*, vol. 281, pp. 189–195, Jul. 2018, doi: 10.1016/J.JCONREL.2018.05.023.

[11]  J. Kwon *et al.*, "Conductive Ink with Circular Life Cycle for Printed Electronics," *Adv. Mater.*, vol. 34, no. 30, p. 2202177, Jul. 2022, doi: 10.1002/ADMA.202202177.

[12]  S. Rasel *et al.*, "Self-Assembled Functionally Graded Graphene Films with Tunable Compositions and Their Applications in Transient Electronics and Actuation," *ACS Appl. Mater. Interfaces*, vol. 11, no. 26, pp. 23463–23473, Jul.

2019, doi: 10.1021/ACSAMI.9B05236/ASSET/IMAGES/LARGE/AM-2019-05236J_0007.JPEG.

[13]  K. S. Novoselov *et al.*, "Electric field in atomically thin carbon films," *Science (80-. ).*, vol. 306, no. 5696, pp. 666–669, Oct. 2004, doi: 10.1126/SCIENCE.1102896/SUPPL_FILE/NOVOSELOV.SOM.PDF.

[14]  J. C. Slonczewski and P. R. Weiss, "Band Structure of Graphite," *Phys. Rev.*, vol. 109, no. 2, p. 272, Jan. 1958, doi: 10.1103/PhysRev.109.272.

[15]  Y. Zhang, Y. W. Tan, H. L. Stormer, and P. Kim, "Experimental observation of the quantum Hall effect and Berry's phase in graphene," *Nat. 2005 4387065*, vol. 438, no. 7065, pp. 201–204, Nov. 2005, doi: 10.1038/nature04235.

[16]  K. Wang, M. Xu, Y. Gu, Z. Gu, J. Liu, and Q. H. Fan, "Low-temperature plasma exfoliated n-doped graphene for symmetrical electrode supercapacitors," *Nano Energy*, vol. 31, pp. 486–494, Jan. 2017, doi: 10.1016/J.NANOEN.2016.11.007.

[17]  K. S. Novoselov *et al.*, "Two-dimensional gas of massless Dirac fermions in graphene," *Nat. 2005 4387065*, vol. 438, no. 7065, pp. 197–200, Nov. 2005, doi: 10.1038/nature04233.

[18]  C. Soldano, A. Mahmood, and E. Dujardin, "Production, properties and potential of graphene," *Carbon N. Y.*, vol. 48, no. 8, pp. 2127–2150, 2010, doi: https://doi.org/10.1016/j.carbon.2010.01.058.

[19]  V. Singh, D. Joung, L. Zhai, S. Das, S. I. Khondaker, and S. Seal, "Graphene based materials: Past, present and future," *Prog. Mater. Sci.*, vol. 56, no. 8, pp. 1178–1271, Oct. 2011, doi: 10.1016/J.PMATSCI.2011.03.003.

[20]  S. Pei and H.-M. Cheng, "The reduction of graphene oxide," *Carbon N. Y.*, vol. 50, no. 9, pp. 3210–3228, 2012, doi: https://doi.org/10.1016/j.carbon.2011.11.010.

[21]  S. Stankovich *et al.*, "Synthesis of graphene-based nanosheets via chemical reduction of exfoliated graphite oxide," *Carbon N. Y.*, vol. 45, no. 7, pp. 1558–1565, Jun. 2007, doi: 10.1016/J.CARBON.2007.02.034.

[22]  H. He, T. Riedl, A. Lerf, and J. Klinowski, "Solid-State NMR Studies of the Structure of Graphite Oxide," *J. Phys. Chem.*, vol. 100, no. 51, pp. 19954–19958, Jan. 1996, doi: 10.1021/jp961563t.

[23]  C. Berger *et al.*, "Ultrathin epitaxial graphite: 2D electron gas properties and a route toward graphene-based nanoelectronics," *J. Phys. Chem. B*, vol. 108, no. 52, pp. 19912–19916, 2004.

[24]  S. Stankovich, R. D. Piner, X. Chen, N. Wu, S. T. Nguyen, and R. S. Ruoff, "Stable aqueous dispersions of graphitic nanoplatelets via the reduction of exfoliated graphite oxide in the presence of poly (sodium 4-styrenesulfonate)," *J. Mater. Chem.*, vol. 16, no. 2, pp. 155–158, 2006.

[25] Y. I. Zhang, L. Zhang, and C. Zhou, "Review of chemical vapor deposition of graphene and related applications," *Acc. Chem. Res.*, vol. 46, no. 10, pp. 2329–2339, 2013.

[26] H. Saleem, M. Haneef, and H. Y. Abbasi, "Synthesis route of reduced graphene oxide via thermal reduction of chemically exfoliated graphene oxide," *Mater. Chem. Phys.*, vol. 204, pp. 1–7, 2018.

[27] H.-H. Huang, K. K. H. De Silva, G. R. A. Kumara, and M. Yoshimura, "Structural evolution of hydrothermally derived reduced graphene oxide," *Sci. Rep.*, vol. 8, no. 1, pp. 1–9, 2018.

[28] R. Y. N. Gengler *et al.*, "Revealing the ultrafast process behind the photoreduction of graphene oxide," *Nat. Commun.*, vol. 4, no. 1, pp. 1–5, 2013.

[29] S. Pei, J. Zhao, J. Du, W. Ren, and H.-M. Cheng, "Direct reduction of graphene oxide films into highly conductive and flexible graphene films by hydrohalic acids," *Carbon N. Y.*, vol. 48, no. 15, pp. 4466–4474, 2010, doi: https://doi.org/10.1016/j.carbon.2010.08.006.

[30] Y. C. Guan, Y. W. Fang, G. C. Lim, H. Y. Zheng, and M. H. Hong, "Fabrication of laser-reduced graphene oxide in liquid nitrogen environment," *Sci. Rep.*, vol. 6, no. 1, pp. 1–7, 2016.

[31] S.-Y. Huang *et al.*, "Enhanced Reduction of Graphene Oxide on Recyclable Cu Foils to Fabricate Graphene Films with Superior Thermal Conductivity," *Sci. Rep.*, vol. 5, no. 1, p. 14260, 2015, doi: 10.1038/srep14260.

[32] J. J. Meister, "MODIFICATION OF LIGNIN*," *J. Macromol. Sci. Part C*, vol. 42, no. 2, pp. 235–289, Jun. 2002, doi: 10.1081/MC-120004764.

[33] A. J. Ragauskas *et al.*, "Lignin valorization: improving lignin processing in the biorefinery," *Science (80-. ).*, vol. 344, no. 6185, p. 1246843, 2014.

[34] A. G. Vishtal and A. Kraslawski, "Challenges in industrial applications of technical lignins," *BioResources*, vol. 6, no. 3, pp. 3547–3568, 2011.

[35] M.-M. Titirici and M. Antonietti, "Chemistry and materials options of sustainable carbon materials made by hydrothermal carbonization," *Chem. Soc. Rev.*, vol. 39, no. 1, pp. 103–116, 2010, doi: 10.1039/B819318P.

[36] J. D. Majumdar and I. Manna, *Laser-assisted fabrication of materials*, vol. 161. Springer Science & Business Media, 2012.

[37] Y. Zhang, H. Gu, and S. Iijima, "Single-wall carbon nanotubes synthesized by laser ablation in a nitrogen atmosphere," *Appl. Phys. Lett.*, vol. 73, no. 26, pp. 3827–3829, 1998.

[38] S. Delacroix, H. Wang, T. Heil, and V. Strauss, "Laser-induced carbonization of natural organic precursors for flexible electronics," *Adv. Electron. Mater.*, vol. 6, no. 10, p. 2000463, 2020.

[39]    T.-R. Cui *et al.*, "Ultrasensitive detection of COVID-19 causative virus (SARS-CoV-2) spike protein using laser induced graphene field-effect transistor," *Molecules*, vol. 26, no. 22, p. 6947, 2021.

[40]    Q. Hong, L. Yang, L. Ge, Z. Liu, and F. Li, "Direct-laser-writing of three-dimensional porous graphene frameworks on indium-tin oxide for sensitive electrochemical biosensing," *Analyst*, vol. 143, no. 14, pp. 3327–3334, 2018.

[41]    S. Luo, P. T. Hoang, and T. Liu, "Direct laser writing for creating porous graphitic structures and their use for flexible and highly sensitive sensor and sensor arrays," *Carbon N. Y.*, vol. 96, pp. 522–531, 2016.

[42]    Q. Tian, W. Yan, Y. Li, and D. Ho, "Bean pod-inspired ultrasensitive and self-healing pressure sensor based on laser-induced graphene and polystyrene microsphere sandwiched structure," *ACS Appl. Mater. Interfaces*, vol. 12, no. 8, pp. 9710–9717, 2020.

[43]    Z. Peng, J. Lin, R. Ye, E. L. G. Samuel, and J. M. Tour, "Flexible and stackable laser-induced graphene supercapacitors," *ACS Appl. Mater. Interfaces*, vol. 7, no. 5, pp. 3414–3419, 2015.

[44]    W. Gao *et al.*, "Direct laser writing of micro-supercapacitors on hydrated graphite oxide films," *Nat. Nanotechnol.*, vol. 6, no. 8, pp. 496–500, 2011.

[45]    W. Zhang, Y. Lei, F. Ming, Q. Jiang, P. M. F. J. Costa, and H. N. Alshareef, "Lignin Laser Lithography: A Direct-Write Method for Fabricating 3D Graphene Electrodes for Microsupercapacitors," *Adv. Energy Mater.*, vol. 8, no. 27, p. 1801840, 2018.

[46]    M. G. Stanford *et al.*, "High-resolution laser-induced graphene. Flexible electronics beyond the visible limit," *ACS Appl. Mater. Interfaces*, vol. 12, no. 9, pp. 10902–10907, 2020.

[47]    T. D. Le *et al.*, "Recent Advances in Laser-Induced Graphene: Mechanism, Fabrication, Properties, and Applications in Flexible Electronics," *Adv. Funct. Mater.*, p. 2205158, 2022.

[48]    M. F. El-Kady and R. B. Kaner, "Scalable fabrication of high-power graphene micro-supercapacitors for flexible and on-chip energy storage," *Nat. Commun.*, vol. 4, no. 1, pp. 1–9, 2013.

[49]    J. Lin *et al.*, "Laser-induced porous graphene films from commercial polymers," *Nat. Commun.*, vol. 5, no. 1, pp. 1–8, 2014.

[50]    H. Liu *et al.*, "Laser-oxidized Fe3O4 nanoparticles anchored on 3D macroporous graphene flexible electrodes for ultrahigh-energy in-plane hybrid micro-supercapacitors," *Nano Energy*, vol. 77, p. 105058, 2020.

[51]    B. Kulyk *et al.*, "Laser-induced graphene from paper for mechanical sensing," *ACS Appl. Mater. Interfaces*, vol. 13, no. 8, pp. 10210–10221, 2021.

[52] M. Yuan *et al.*, "Facile and scalable fabrication of high-performance microsupercapacitors based on laser-scribed in situ heteroatom-doped porous graphene," *ACS Appl. Mater. Interfaces*, vol. 13, no. 19, pp. 22426–22437, 2021.

[53] M. Yuan *et al.*, "Laser synthesis of superhydrophilic O/S co-doped porous graphene derived from sodium lignosulfonate for enhanced microsupercapacitors," *J. Power Sources*, vol. 513, p. 230558, 2021.

[54] Y. Lei, A. H. Alshareef, W. Zhao, and S. Inal, "Laser-Scribed Graphene Electrodes Derived from Lignin for Biochemical Sensing," *ACS Appl. Nano Mater.*, vol. 3, no. 2, pp. 1166–1174, Feb. 2020, doi: 10.1021/acsanm.9b01795.

[55] S. Evlashin *et al.*, "Controllable Laser Reduction of Graphene Oxide Films for Photoelectronic Applications," *ACS Appl. Mater. Interfaces*, vol. 8, no. 42, pp. 28880–28887, Oct. 2016, doi: 10.1021/acsami.6b10145.

[56] T. X. Tran *et al.*, "Laser-induced reduction of graphene oxide by intensity-modulated line beam for supercapacitor applications," *ACS Appl. Mater. Interfaces*, vol. 10, no. 46, pp. 39777–39784, 2018.

[57] J.-X. Yan *et al.*, "Highly Conductive Graphene Paper with Vertically Aligned Reduced Graphene Oxide Sheets Fabricated by Improved Electrospray Deposition Technique," *ACS Appl. Mater. Interfaces*, vol. 11, no. 11, pp. 10810–10817, Mar. 2019, doi: 10.1021/acsami.8b19811.

[58] B. Jiang *et al.*, "Lignin as a wood-inspired binder enabled strong, water stable, and biodegradable paper for plastic replacement," *Adv. Funct. Mater.*, vol. 30, no. 4, p. 1906307, 2020.

[59] Y. Chyan, R. Ye, Y. Li, S. P. Singh, C. J. Arnusch, and J. M. Tour, "Laser-induced graphene by multiple lasing: toward electronics on cloth, paper, and food," *ACS Nano*, vol. 12, no. 3, pp. 2176–2183, 2018.

[60] S. Park *et al.*, "Fabrication of fanlike L-shaped graphene nanostructures with enhanced thermal/electrochemical properties via laser irradiation," *Carbon N. Y.*, vol. 182, pp. 691–699, 2021.

[61] M. J. McAllister *et al.*, "Single sheet functionalized graphene by oxidation and thermal expansion of graphite," *Chem. Mater.*, vol. 19, no. 18, pp. 4396–4404, 2007.

[62] M. Yan, W. Huang, and Z. Li, "Chitosan cross-linked graphene oxide/lignosulfonate composite aerogel for enhanced adsorption of methylene blue in water," *Int. J. Biol. Macromol.*, vol. 136, pp. 927–935, 2019.

[63] L. M. Malard, M. A. Pimenta, G. Dresselhaus, and M. S. Dresselhaus, "Raman spectroscopy in graphene," *Phys. Rep.*, vol. 473, no. 5–6, pp. 51–87, 2009.

[64] M. Hepp *et al.*, "Trained laser-patterned carbon as high-performance mechanical sensors," *npj Flex. Electron.*, vol. 6, no. 1, p. 3, Dec. 2022, doi: 10.1038/s41528-022-00136-0.

[65] F. M. Smits, "Measurement of sheet resistivities with the four-point probe," *Bell Syst. Tech. J.*, vol. 37, no. 3, pp. 711–718, 1958.

[66] J. Y. Hwang *et al.*, "Direct preparation and processing of graphene/RuO2 nanocomposite electrodes for high-performance capacitive energy storage," *Nano Energy*, vol. 18, pp. 57–70, 2015.

[67] J. Cai, A. Watanabe, and C. Lv, "Laser direct writing of carbon/Au composite electrodes for high-performance micro-supercapacitors," in *Laser-based Micro- and Nanoprocessing XI*, 2017, vol. 10092, pp. 123–130.

[68] V. B. Nam, J. Shin, A. Choi, H. Choi, S. H. Ko, and D. Lee, "High-temperature, thin, flexible and transparent Ni-based heaters patterned by laser-induced reductive sintering on colorless polyimide," *J. Mater. Chem. C*, vol. 9, no. 17, pp. 5652–5661, 2021.

[69] H. Wang *et al.*, "Laser-carbonization: Peering into the formation of micro-thermally produced (N-doped) carbons," *Carbon N. Y.*, vol. 176, pp. 500–510, 2021.

[70] Y. Li *et al.*, "Laser-induced graphene in controlled atmospheres: from superhydrophilic to superhydrophobic surfaces," *Adv. Mater.*, vol. 29, no. 27, p. 1700496, 2017.

[71] A. Balakrishnan, W. D. Palmer, W. T. Joines, and T. G. Wilson, "The inductance of planar structures," in *Proceedings Eighth Annual Applied Power Electronics Conference and Exposition,* 1993, pp. 912–921.

[72] H. M. Greenhouse, "Design of planar rectangular microelectronic inductors," *IEEE Trans. parts, hybrids, Packag.*, vol. 10, no. 2, pp. 101–109, 1974.

[73] S. S. Mohan, M. del Mar Hershenson, S. P. Boyd, and T. H. Lee, "Simple accurate expressions for planar spiral inductances," *IEEE J. Solid-State Circuits*, vol. 34, no. 10, pp. 1419–1424, 1999.

[74] X. Ding, Y. Pu, M. Tang, and T. Zhang, "Environmental and health effects of graphene-family nanomaterials: potential release pathways, transformation, environmental fate and health risks," *Nano Today*, vol. 42, p. 101379, 2022.

[75] L. Teng, S. Ye, S. Handschuh-Wang, X. Zhou, T. Gan, and X. Zhou, "Liquid metal-based transient circuits for flexible and recyclable electronics," *Adv. Funct. Mater.*, vol. 29, no. 11, p. 1808739, 2019.